Journal of Nanobiotechnology

RESEARCH

Open Access

A spreadable self-gelling hemostatic powder sensitizes CAR-NK cell therapy to prevent hepatocellular carcinoma recurrence postresection

Yusheng Cheng[1,2,3†], Yihang Gong[4,5†], Xin Li[1,2,3†], Fanxin Zeng[4,5†], Bo Liu[1,2,3†], Wenjie Chen[6], Feng Zhang[6], Haofei Chen[3], Weixiong Zhu[1], Hui Li[7*], Lei Zhou[8*], Tiangen Wu[9,10*] and Wence Zhou[1,2,3*]

Abstract

Adoptive natural killer cell therapy (ANKCT) harbors great potential for combating postsurgical hepatocellular carcinoma (HCC) recurrence, but its efficacy is limited by tumor microenvironment (TME)-meditated repression on NK cell function and insufficient NK cell homing to tumor sites. Therefore, herein we develop a nanocomposite sprayable self-gelling powder enabling liver-localized codelivery of three FDA-approved drugs including calcitriol (Cal), gemcitabine (Gem), and tazemetostat (Taz) to address these challenges. This powder can be laparoscopically spread to liver wound sites, where it rapidly absorbs interfacial liquid to form a bulk adhesive pressure-resistant hydrogel in situ, implying its application potential in minimally surgery. Moreover, its application to liver resection bed significantly sensitizes allogenic NK and EpCAM chimeric antigen receptor modified-NK-92 (EpCAM-CAR-NK) cell infusion to prevent HCC recurrence in orthotopic Heap1-6 tumor-bearing and patient-derived tumor xenograft (PDX) HCC murine models. Additionally, this powder can allow for an effective hemostatic effect in rat and porcine models due to its powerful tissue adhesion-seal and erythrocyte-aggregating effects. Altogether, our newly developed hemostatic self-gelling powder can significantly sensitize ANKCT to combat HCC recurrence in a manner compatible with surgical treatment of HCC.

†Yihang Gong, Yusheng Cheng, Xin Li, Fanxin Zeng, and Bo Liu contributed equally to this work.

*Correspondence:
Hui Li
lih@cqu.edu.cn
Lei Zhou
zhoul@gzhmu.edu.cn
Tiangen Wu
wtg666@whu.edu.cn
Wence Zhou
zhouwc129@163.com

Full list of author information is available at the end of the article

Graphical abstract

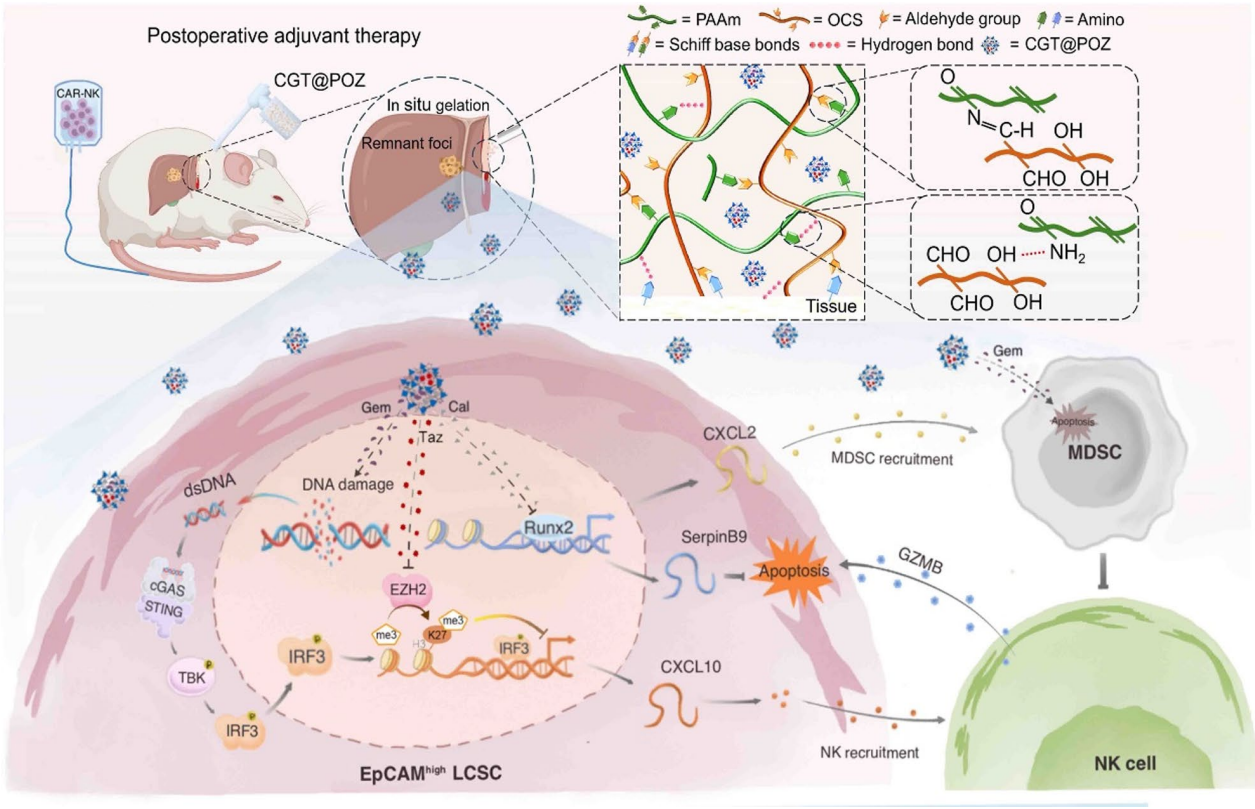

Keywords Nanocomposite hydrogel, Drug delivery, Hemostasis, Hepatocellular carcinoma, NK cell therapy

Introduction

Hepatocellular carcinoma (HCC) is the second predominant root of cancer-associated death globally [1, 2]. The surgical resection remains the preferred choice for HCC patients due to its curative potential [3, 4]. Nonetheless, HCC recurrence occurs in approximately half of cases within postoperative 2 years, which seriously impairs long-term survival prognosis of patients. Worse still, no effective therapies are currently available to prevent HCC recurrence in clinical practice. Recent evidence suggests that adoptive natural killer cell therapy (ANKCT) shows great potential for preventing postsurgical HCC recurrence, but its efficacy is limited by tumor microenvironment (TME)-meditated repression on NK cell function and insufficient NK cell homing to tumor masses [5]. Therefore, more and more researches are launched to explore ANKCT-based combination therapeutic strategies against HCC recurrence postresection.

Liver cancer stem cells highly expressing epithelial cell adhesion molecule (EpCAM^{high} LCSCs) represent one of key cellular components of HCC TME and have been proposed as the cellular seeds of postoperative HCC recurrence [6]. Of note, EpCAM^{high} LCSCs can resist NK cell-meditated cell lysis, though the relevant mechanisms are largely elusive [7]. In this article, we initially reveal that RUNX family transcription factor 2 (Runx2) promotes EpCAM^{high} LCSC resistance to NK cell-meditated cell lysis via transcriptionally upregulating SerpinB9, an inhibitor of granzyme B-induced apoptosis [8]. In contrast, Runx2 inhibition by calcitriol (Cal), an FDA-approved drug for osteoporosis, can dramatically sensitize EpCAM^{high} LCSCs to NK cell killing. Apart from LCSCs, diverse immunosuppressive cells, such as tumor-associated macrophages (TAM), regulatory T cells (Treg), and myeloid-derived suppressor cells (MDSC), in TME also exert an inhibitory effect on NK cell antitumor immunity [9]. Particularly, MDSCs can not only cause NK cell dysfunction in a direct manner, but also impair NK cell function through facilitating the expansion and recruitment of TAMs and Tregs [10]. In addition, hepatectomy-induced stress can largely expand MDSCs in patients with HCC [11]. Moreover, adoptive NK cell transfer itself may drive MDSC recruitment into tumor sites [12]. Obviously, these clues support that

MDSCs hold a dominant position in immunosuppressive immune cell-mediated NK cell dysfunction in the context of hepatectomy plus ANKCT. Intriguingly, our data confirms that calcitriol and gemcitabine (Gem), a common DNA damage-inducing chemotherapy drug, can cooperate to mitigate MDSC accumulation in HCC through reducing MDSC recruitment and inducing MDSC apoptosis, respectively. C-X-C motif chemokine ligand 10 (CXCL10) has been disclosed to occupy a central role in NK cell homing to HCC as NK cell chemokine [13]. However, its expression is often repressed epigenetically by histone H3 lysine 27 methyltransferase Enhancer of zeste homolog 2 (EZH2) in HCC cells. On contrast, in this study we demonstrate that EZH2 inhibitor tazemetostat (Taz), an FDA-approved drug against refractory lymphoma, can significantly enhance NK cell homing to HCC via epigenetic upregulation of CXCL10 expression. Moreover, gemcitabine can sensitize tazemetostat to increase CXCL10 expression in HCC cells, mainly due to its activating cyclic GMP-AMP synthase-stimulator of interferon genes (cGAS-STING) pathway [14]. Therefore, ANKCT plus a cocktail of Cal, Gem, and Taz may represent an effective strategy against HCC recurrence postresection.

The clinical application of multidrug combination is often hindered by limited intratumoral accumulation of drugs and off-target toxicities [15]. The tumor-localized drug delivery has been proposed as promising strategies to increase intratumoral drug accumulation through avoiding long-distance delivery routes and mitigate drug-related systemic toxicities resulting from drug absorption by other organs [16]. In addition, applying hemostatic agents to prevent bleeding after surgical resection of solid tumors is a common clinical practice. In these contexts, we have previously developed the injectable hemostatic hydrogels as local drug depots for augmenting ANKCT efficacy after surgical resection of solid tumors including HCC [5, 17]. However, our developed hydrogels or similar hydrogels designed by other research teams are in a liquid state or liquid-hydrogel transition state prior to their application to surgical bed or cavity, so they own a low capacity of absorbing interfacial blood [18]. This drawback will lead to poor hydrogel-tissue interfaces and biomechanical instability of hydrogels, resultantly discounting their therapeutic performance. To solve this problem, herein we develop a nanocomposite sprayable self-gelling powder for enabling liver-localized codelivery of Cal, Gem, and Taz. In detail, we first prepared freeze-dried polyacrylamide (PAAm) hydrogel, oxidized chondroitin sulfate (OCS), and zeolitic imidazolate framework-8 (ZIF-8) nanoscale particles encapsulating Cal, Gem, and Taz. Then, we mixed and ground freeze-dried PAAm hydrogel, OCS, and ZIF-8 nanoparticles to obtain a nanocomposite powder, thereafter referred to as CGT@POZ powder (Fig. 1). This powder can be laparoscopically sprayed to liver wound sites, where it rapidly absorbs interfacial liquid and then forms a bulk adhesive pressure-resistant hydrogel in situ, indicating its application potential in minimally surgery. Moreover, its application to liver resection bed can effectively sensitize allogenic NK and EpCAM chimeric antigen receptor modified-NK-92 cell (EpCAM-CAR-NK) therapy to prevent HCC recurrence in orthotopic Heap1-6 tumor-bearing and patient-derived tumor xenograft (PDX) HCC murine models. In addition, this powder can generate a prompt and effective hemostatic effect in rat and porcine models, due to its powerful tissue adhesion-seal and erythrocyte-aggregating effects. Altogether, our work provides proof-of-concept that a sprayable hemostatic self-gelling powder for enabling liver-localized codelivery of Cal, Gem, and Taz to improve ANKCT efficacy in preventing HCC recurrence postresection.

Materials and methods

Human tumor specimens

The tumor tissue samples were obtained from 100 participants treated by hepatectomy for HCC at the Third Affiliated Hospital, Sun Yat-sen University, between February 2015 and December 2016. The written informed consents were given by all participants. This work was carried out under the approval from the Ethics Review Board of the Third Affiliated Hospital, Sun Yat-sen University (Approval no. II2024-166-01).

Cell culture

Huh-7 cells, Hepa1-6 cells and NK-92 cells were procured from the American Typical Culture Collection (ATCC). Primary murine NK cells were isolated using a Mojosort Mouse NK Cell Isolation Kit (Biolegend, Cat#480049). Tumor cells were grown in Dulbecco's Modified Eagle's Medium which contains 10% fetal bovine serum (FBS) as well as 0.1% penicillin-streptomycin. NK-92 cells and original murine NK cells were cultivated with IL-2 (10 ng/ml). The cell cultivation y was performed under the condition of 37 °C and 5% CO2.

Establishment of EpCAM-CAR-NK

To obtain EpCAM-CAR-NK cells, a second-generation CAR, which consists of an EpCAM-specific scFv linked to CD8 hinge and transmembrane domains followed by the intracellular signaling domains of 4-1BB and CD3ζ in sequence, was first constructed. Then, this CAR was inserted into a lentiviral vector system containing sequences encoding green fluorescent protein (GFP). Subsequently, NK-92 cell lines were transduced with EpCAM-specific CAR to generate EpCAM-CAR-NK-92.

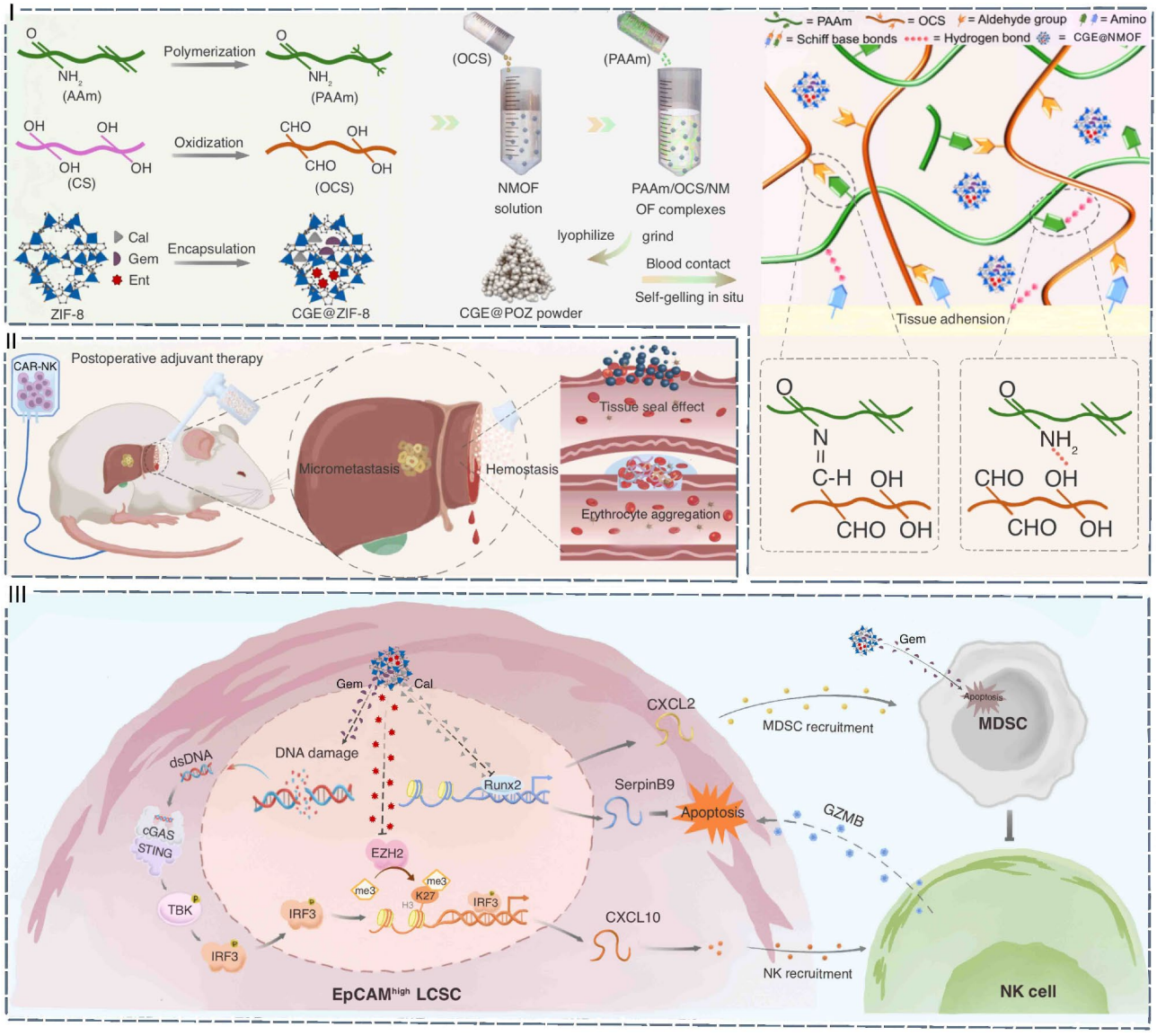

Fig. 1 Schematic of CGT@POZ powder preparation and its enhancement on adoptive NK cell therapy to prevent HCC recurrence. The freeze-dried polyacrylamide (PAAm) hydrogel, oxidized chondroitin sulfate (OCS), and zeolitic imidazolate framework-8 (ZIF-8) nanoparticles loaded with Calcitriol (Cal), Gemcitabine (Gem), and tazemetostat (Taz) were first prepared. Then, they are mixed and ground to obtain a nanocomposite powder, thereafter referred to as CGT@POZ powder. Once sprayed to liver resection margin, CGT@POZ powder rapidly forms an adhesive pressure-resistant hydrogel in situ, which can not only generate a rapid hemostasis but also sustain a liver-localized release of Cal, Gem, and Taz. After delivered into micrometastasis or remnant tumor foci, these drugs can cooperatively sensitize adoptive NK cell therapy to prevent postsurgical hepatocellular carcinoma (HCC) recurrence. Mechanistically, Cal reverses the resistance of liver cancer stem cells highly expressing epithelial cell adhesion molecule to NK cell-meditated cell lysis. Cal and Gem cooperatively decrease MDSC accumulation in HCC through reducing MDSC recruitment and killing MDSCs, thus maintaining NK cell function. Taz and Gem generate a synergistic effect in boosting NK cell homing to HCC by epigenetically and transcriptionally upregulating CXCL10 expression in HCC cells

Synthesis of PAAm hydrogel

To synthesize PAAm hydrogel, we first mixed AAm in deionized water solution and ammonium persulfate in deionized water solution. Then, we heated the mixture in water bath (70℃, 30 min) to generate PAAm hydrogel, which was freeze-dried for further use.

Synthesis and characterization of ZIF-8 nanoparticles

To prepare ZIF-8 nanoscale particles, we first dissolved 325 mg of 2-methylimidazole (2-MIM) in methanol (10 mL) and then stirred the mixture at room temperature for half an hour to obtain a uniform solution, thereafter termed as solution A. In addition, we added 147 mg of zinc nitrate hexahydrate into methanol (5 mL) at room temperature and subsequently subjected the mixture

to 5 min ultrasonic vibration, ultimately generating the homogenous solution (solution B). Next, we added solution A into solution B drop by drop, and stirred the mixture sufficiently (1500 rpm) at 37 °C for 30 min. At the final step, the solution was lyophilized to form ZIF-8 nanoparticle powder. The dimension of ZIF-8 nanoparticles was determined using a Malvern Nano-ZS 90 laser instrument (Worcestershire, UK). The transmission electron microscope (JSM-7500 F, JEOL, Japan) was applied to examine the morphology of ZIF-8 nanoparticles. The powder X-ray diffraction (PXRD) analysis was carried out to ascertain the crystalline structure of ZIF-8 nanocomposites.

Drug-loading efficiency of ZIF-8 nanoparticles

To explore the drug-loading capacity of ZIF-8 nanocomposites, we first labelled drugs (Cal, Gem or Taz) with fluorescein isothiocyanate (Cy5.5). Then, we dissolved Cal, Gem or Taz in PBS (pH 7.4) in each independent experiment, and subsequently added 1 mg ZIF-8 nanoparticles in drug solutions. Next, we stirred the mixture intensely for one day at ambient temperature. After agitation, we separated the supernatant through centrifugating the solution at 9000 rpm for 10 min. The sediment was softly washed two times using 10 ml of deionized water to remove any remaining drugs. In particular, the deionized water was added to the collected supernatant. The drug solutions prior to drug loading and those solutions after drug loading procedure were analyzed via a UV-vis spectrophotometer (Lambda 35, PerkinElmer) at a wavelength of 673 nm, which helps to calculate the amount of drug encapsulated into ZIF-8 nanoparticles. The calculation of drug loading capacity was implemented based on the equation: (M0-M1)/M × 100%, where M0 means the entire drug mass, and M1 signifies the drug mass existing in the supernatant after the loading procedure, and M stands for the mass of drug-loaded ZIF-8 nanoparticles.

Production of oxidized chondroitin sulfate

The oxidized chondroitin sulfate (OCS) powder was produced by the reported protocol [19]. Initially, we dissolved 1.25 g of CS in 20 milliliters of distilled water, which was constantly stirred at 4 °C. When CS was fully dissolved, we further added 1.93 g of sodium periodate into the solution, and put the mixture in darkness for 6 h. Subsequently, the mixture was placed onto a dialysis membrane with a molecular weight cut-off of 3500 and dialyzed against 2 L distilled water for one day at room temperature, in which distilled water was replaced every 6 h. After dialysis, the mixture was transferred into a 50 ml centrifuge tube, frozen at -20 °C for one day, and subsequently lyophilized for over one week to obtain OCS powder.

Preparation and characterization of CGT@POZ hydrogel

To prepare CGT@POZ hydrogel, we first mixed and ground freeze-dried PAAm hydrogel, OCS powder, and ZIF-8 nanocomposites loading with Cal, Gem, and Taz to obtain CGT@POZ powder. Then, PBS at 37 °C was added to CGT@POZ powder to generate CGT@POZ hydrogel. The chemical composition of hydrogel was investigated by Fourier transform infrared analysis and element mapping analysis. Its morphology was observed using scanning electron microscopy. The distribution of drugs labelled with Cy5.5 in the hydrogel was analyzed using a confocal microscope (Zeiss LSM 710).

Evaluation of hemostasis performance

The massive hemorrhage model in porcine was applied to evaluate the hemostasis performance of CGT@POZ powder as previously described [20]. In brief, the wounds with the length of 2 cm and depth of 1 cm in the spleen and liver of 20–25 kg small-scale pigs ($n = 6$) were first created, respectively. Then, we deposited the commercial chitosan powder (500 mg) or CGT@POZ powder (200 mg) onto the bleeding sites. This experiment was approved by the endorsement of the Animal Care and Use Committee of Huateng BioScience (C202304-14).

Antitumor effects of CGT@POZ powder in animal models

To explore the efficacy of CGT@POZ powder treatment in preventing HCC recurrence post-resection, we first established orthotopic Hepa1-6 tumor-bearing models in a total of 60 Balb/c mice as we previously described [5]. Briefly, 50 μL of Hepa1-6 cells (2×10^6 cells) were seeded into the left hepatic lobe on day 0. The tumor formation in each mouse was confirmed on day 5 by the in vivo bioluminescence imaging technique. Then, we removed the tumor of left liver lobe, with a distance of approximately 1 mm from the tumor edge to the surgical margin. Subsequently, these mice were randomized into 10 groups: group 1 for applying chitosan powder to liver resection margin (G1, Control) on day 10, group 2 for applying POZ powder (G2, POZ), group 3 for applying C@POZ powder (G3, C@POZ), group 4 for applying G@POZ powder (G4, G@POZ), group 5 for applying T@POZ powder (G5, T@POZ), group 6 for applying CG@POZ powder (G6, CG@POZ), group 7 for applying GT@POZ powder (G7, GT@POZ), group 8 for applying CT@POZ powder (G8, CT@POZ), group 9 for intravenous injection of Cal, Gem, and Taz (G9, CGT-iv), and group 10 for applying CGT@POZ powder (G10, CGT@POZ). To determine whether CGT@POZ powder treatment enhances adoptive NK cell therapy (ANKCT) to prevent HCC recurrence post-resection, a total of 18 Hepa1-6 cell-HCC murine models were first subjected to surgical resection of the primary tumor and then randomly divided into 3 groups: group 1 for applying chitosan

powder to liver resection margin (designated as control group), group 2 for adoptive allogenic NK cell therapy on day 7 (NK), and group 3 for CGT@POZ powder treatment on day 5 followed by NK cell therapy on day 7 (CGT@POZ-NK). To further investigate whether CGT@POZ powder treatment improves ANCT efficacy, we first established a total of 20 immune-humanized NOD scid gamma (NSG) mice and used them to create orthotopic patient-derived xenograft (PDX) HCC models as previously described [21]. These mice were subsequently allocated into 4 groups in a random manner: group 1 for no treatments (Control), group 2 for unmodified NK-92 cell therapy (NK), group 3 for EpCAM-CAR-NK-92 cell therapy (CAR-NK), and group 4 for applying CGT@POZ powder treatment and EpCAM-CAR-NK-92 cell therapy (CGT@POZ-CAR-NK). After treatment for three weeks, the micro-computed tomography scanning was performed to examine the tumor volumes in each group. These studies received the endorsement of the Animal Care and Use Committee of Jennio Biotech Co.,Ltd (IACUC-2023-A039).

Flow cytometry analysis of immune cells

Tumor tissues and spleen tissue were processed in complete 1640 culture medium with the addition of 0.5 mg/ml of collagenase-IV (Sigma-Aldrich, Cat# C5138), 0.1 mg/ml of DNase-I (Sigma-Aldrich, Cat# DN25) and 0.1 mg/ml of Hyaluronidase Type V (Sigma-Aldrich, Cat# H6254), and incubated at 37 °C for an hour. By compressing the enzymatically treated tissues through a 40 μm mesh using a syringe's plunger, a homogeneous suspension of individual cells was achieved. Then, tumor-infiltrated immune cells (TIICs) were isolated via differential speed centrifugation from single-cell suspensions. The suspensions of TIICs were subjected to flow cytometry analysis as previously published. The antibodies used in flow cytometry analysis are as follows: anti-CD45-PE/CY7 (BioLegend, Cat#103114), anti-TNF-α-EF450 (Ebioscience, Cat#48-7321-82), anti-NKP46-EF450(Ebioscience, Cat#48-3351-82), anti-GR1-APC (BioLegend, Cat#108412), anti-CD11b-FITC (BioLegend, Cat#101206), anti-NKp46-APC (BioLegend, Cat#137608), anti-GZMB-EF450 (Ebioscience, Cat#48-8898-82), anti-CD11c-PB(BioLegend, Cat#117322).

Statistical analysis

GraphPad Prism V.7 and IBM SPSS Statistics V.20 were used to analyze the data. The statistical tests used for data analysis included Student's t test, One-way repeated-measures ANOVA test, and the log-rank test. The survival analysis was performed by the Kaplan-Meier analysis. $p < 0.05$ indicated significance.

Results and discussion

Calcitriol and gemcitabine cooperatively mitigate HCC microenvironment-meditated Inhibition on NK cell function

NK cell antitumor immunity impairment has been confirmed as one of pivotal reasons for postoperative HCC recurrence, indicating that ANKCT may show promise in preventing this vicious event [22]. However, when applied as monotherapy, ANKCT can only improve survival prognosis to a limited extent without effect in lowering the incidence of HCC recurrence postresection [5, 23]. Increasing evidence confirms that TME-meditated inhibition on NK cell function is a crucial cause of limited ANKCT efficacy in solid tumors [24]. Liver cancer stem cells highly expressing epithelial cell adhesion molecule ($EpCAM^{high}$ LCSCs), which have been proposed as the cellular seeds of postoperative HCC recurrence, represent a key cellular component of HCC TME [6]. Remarkably, $EpCAM^{high}$ LCSCs are naturally resistant to NK cell-meditated cell lysis [7]. Consistent with previous evidence, our data also demonstrates that $EpCAM^{high}$ Huh-7 cells display typical stem-like properties (Fig. 2a-c) and exhibit rather low sensitivity to NK cell-mediated cell lysis in comparison with $EpCAM^{low}$ Huh-7 cells (Figure S1). Therefore, it is imperative to decipher how $EpCAM^{high}$ LCSCs resist NK cell killing and then develop ANKCT-based combination therapy for preventing HCC recurrence postresection.

Runt-related transcription factor 2 (Runx2) is a renowned regulator of human osteoblast differentiation and chondrocyte maturation [25]. Recent evidence uncovers that Runx2 is highly expressed in HCC and acts as an oncogene. In particular, Runx2 plays an essential role in promoting the stemness of breast cancer [26] and colorectal cancer [27]. Similarly, our quantitative real-time PCR (qRT-PCR) analysis verifies that Runx2 has much higher expression level in $EpCAM^{high}$ LCSCs than in $EpCAM^{low}$ Huh-7 cells (Figure S2). In addition, immunofluorescence staining analysis identifies an elevated nuclear accumulation of Runx2 in $EpCAM^{high}$ LCSCs (Fig. 2d). In addition, there is a positive relationship between Runx2 and EpCAM expressions in resected human HCC tissues (Fig. 2e & Figure S3a). Moreover, our Kaplan-Meier survival analysis shows that higher Runx2 expression is closely correlated with worse recurrence-free survival of HCC patients (Figure S3b). Importantly, an inverse correlation between Runx2-positive cell number and activated NK cell ($CD56^{+}NKP44^{+}$) number in clinical HCC specimens was observed (Fig. 2f-g). Based on these clues, we further asked whether Runx2 is implicated in $EpCAM^{high}$ LCSC resistance to NK cell-mediated cell lysis. As shown in Fig. 2h & Figure S4a-b, Runx2 knockdown can dramatically sensitize NK cells to kill $EpCAM^{high}$ LCSCs, indicating that Runx2 promotes

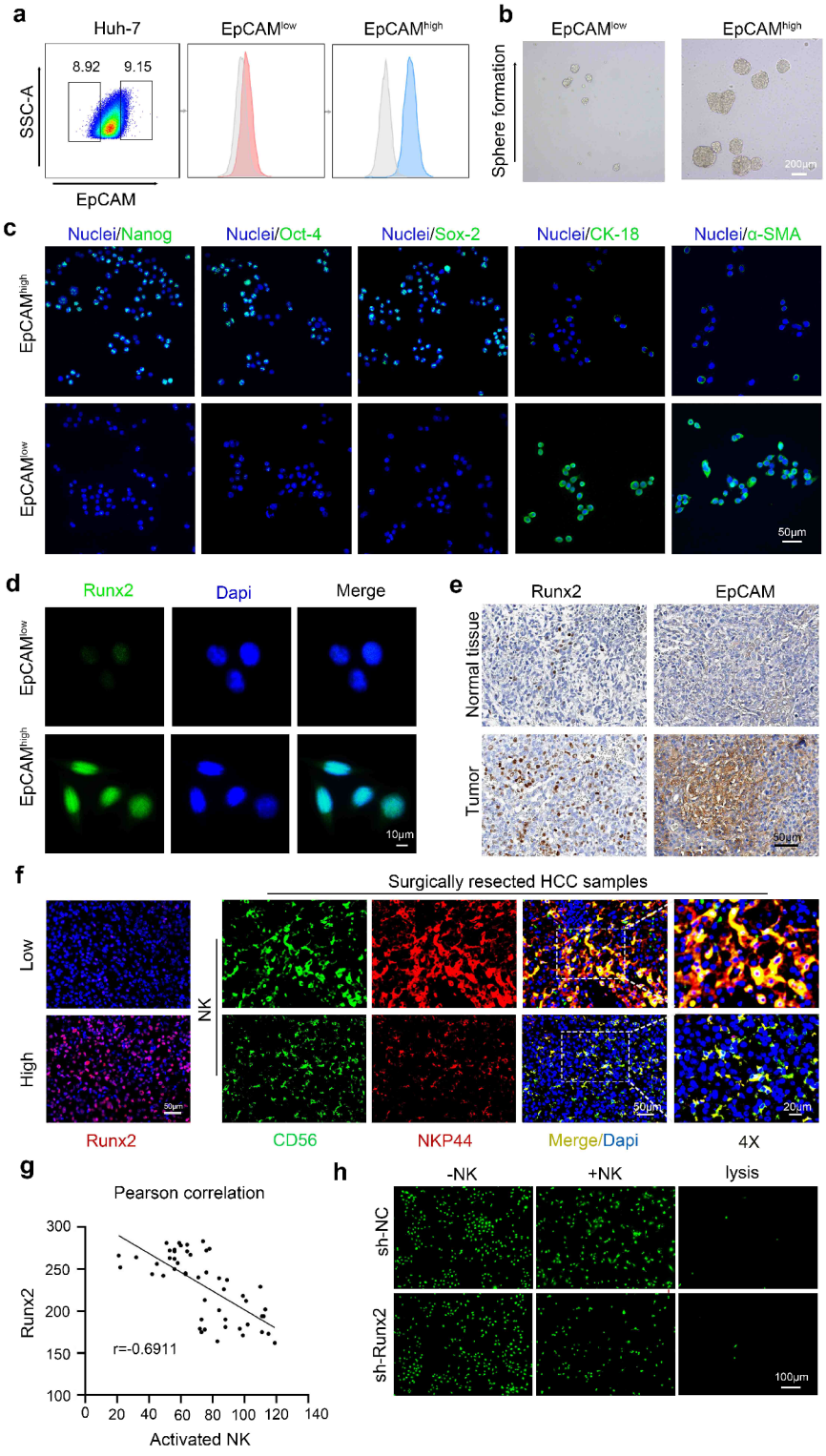

Fig. 2 Runx2 promotes the resistance of EpCAM^{high} LCSCs to NK cell-meditated cell lysis. **a**: Isolation of EpCAM^{high} and EpCAM^{low} cell subsets from Huh-7 cell lines through flow cytometry. **b**: Sphere formation by EpCAM^{high} and EpCAM^{low} Huh-7 cells in stem cell medium, scale bar = 200 μm. $n = 3$. **c**: Immunofluorescence staining of Nanog, Oct-4, Sox-2, CK-18, and α-SMA in EpCAM^{high} and EpCAM^{low} cells, scale bar = 20 μm. $n = 3$. **d**: Immunofluorescence stain of EpCAM and Runx2 in EpCAM^{low} and EpCAM^{high} Huh-7 cells. **e**: Immunohistochemical analysis of Runx2 and EpCAM expressions in resected HCC specimens from patients. **f**: Immunofluorescence analysis of the correlation between Runx2-positive cell number and activated NK cell (CD56^{+}NKP44^{+}) number in surgically resected HCC specimens. **g**: Pearson correlation analysis of the correlation between Runx2-positive cell number and activated NK cell (CD56^{+}NKP44^{+}) number in HCC specimens. r values of b were calculated using a Pearson correlation test. **h**: Calcein AM cytotoxicity assay shows that Runx2 knockdown reverses EpCAM^{high} Huh-7 cell resistance to NK cell-meditated lysis. $n = 3$

EpCAM^{high} LCSC resistance to NK cell-meditated cell lysis.

Granzyme B (GZMB) is a critical NK cell effector molecule inducing tumor cell apoptosis. Coincidently, our RNA-seq analysis shows that Runx2 knockdown significantly downregulates SerpinB9, an inhibitor of GZMB-induced apoptosis [8] (Fig. 3a-b). Hence, we further explored whether Runx2 promotes the resistance of EpCAM^{high} LCSCs to NK cell-meditated cell lysis via transcriptional activation of SerpinB9 expression. To achieve this, qRT-PCR and western blotting analyses were conducted to examine SerpinB9 expression levels. The results confirm that Runx2 knockdown can dramatically reduce SerpinB9 expression in mRNA and protein levels (Fig. 3c-d). In addition, our dual-luciferase reporter assay shows that Runx2 knockdown substantially mitigates the luciferase activity driven by the SerpinB9 promoter, indicating the direct binding of Runx2 to the SerpinB9 promoter (Fig. 3e). Moreover, Runx2 knockdown significantly sensitized EpCAM^{high} LCSCs to NK cell-mediated cell lysis, and this effect was dramatically attenuated by SerpinB9 overexpression (Fig. 3f-h). Inversely, Runx2 overexpression markedly promoted EpCAM^{high} LCSCs to resist NK cell killing (Figure S5). Obviously, these findings support that Runx2 can facilitate EpCAM^{high} LCSC resistance to NK cell-meditated cell lysis via transcriptional activation of SerpinB9 expression. Calcitriol (Cal), an FDA-approved drug for osteoporosis, has been revealed as a Runx2 inhibitor [28]. Therefore, we further investigated the effect of Cal on EpCAM^{high} LCSC resistance to NK cell-meditated cell lysis. As shown in Fig. 3i-j, Cal significantly reduces Runx2 and SerpinB9 expressions in EpCAM^{high} LCSCs, and Runx2 overexpression can abrogate Cal-meditated inhibition on SerpinB9 expression. Moreover, Cal-pretreated EpCAM^{high} LCSCs are significantly sensitive to NK cell killing (Fig. 3k & Figure S6a-b). Similar to EpCAM^{high} Huh-7 cells, EpCAM^{high} Hepa1-6 cells also possess the stem-like properties and are resistant to NK cell-meditated cell lysis. Expectedly, pretreatment by Cal also substantially abrogates EpCAM^{high} Hepa1-6 cell resistance to NK cell killing (Figure S6c).

In addition to tumor cells, a multiple of immunosuppressive cells, such as tumor-associated macrophages (TAM), regulatory T cells (Treg), and myeloid-derived suppressor cells (MDSC) in HCC TME, can also strongly inhibit NK cell function. Particularly, MDSCs can not only cause NK cell dysfunction in a direct manner, but also impair NK cell function indirectly through boosting the expansion and recruitment of TAMs and Tregs [10]. Besides, hepatectomy-induced stress can largely expand MDSCs in HCC patients via intricate mechanisms. More importantly, adoptive NK cell transfer itself has been disclosed to promote MDSC recruitment into HCC [12]. These clues suggest that MDSCs may hold a dominant position in immunosuppressive immune cell-meditated NK cell dysfunction in the context of hepatectomy followed by ANKCT. It has been demonstrated that gemcitabine (Gem), an FDA-approved chemotherapeutic agent for advanced HCC, can kill intratumoral MDSCs in a multiple of solid tumors [29–31]. Therefore, we explored the effect of Gem on MDSC accumulation in HCC though flow cytometry analysis. The gating strategy for identifying murine MDSCs is presented in Figure S7a. As expected, Gem also significantly reduces MDSC accumulation in orthotopic Hepa1-6 tumor-bearing murine model (Fig. 3l & Figure S8). Of note, our RNA-seq analysis shows that Runx2 knockdown significantly downregulates the expression of MDSC chemokine CXCL2 in EpCAM^{high} LCSCs, which is validated by ELISA analysis (Fig. 3a-b & Figure S9a). Furthermore, Cal can also substantially decrease CXCL2 expression in EpCAM^{high} LCSCs, whereas Runx2 overexpression significantly mitigates this effect (Figure S9b). Meanwhile, pretreatment by Cal significantly impedes EpCAM^{high} Hepa1-6 cells from recruiting MDSCs in vitro, which is markedly reversed by Runx2 overexpression (Fig. 3m & Figure S9c). Therefore, we further asked whether Cal and Gem cooperatively reduce the infiltration of MDSCs in HCC. As presented in Fig. 3l, Gem and Cal can generate a synergistic inhibition on MDSC accumulation in orthotopic Hepa1-6 tumor-bearing murine model. Altogether, Cal and Gem can cooperatively relieve HCC microenvironment-meditated inhibition on NK cell function, indicating their potential as promising candidate drugs for ANKCT-based combination therapy against HCC recurrence postresection.

Tazemetostat and gemcitabine synergistically enhance NK cell homing to HCC

Apart from TME-mediated suppression on NK cell function, insufficiency of NK cell homing to tumor sites also severely limits ANKCT efficacy in solid tumors. C-X-C motif chemokine ligand 2 (CXCL10) is a kind of NK cell chemokines and occupies a central role in promoting NK cell homing to HCC [13]. However, its expression is epigenetically repressed by histone H3 lysine 27 methyltransferase Enhancer of zeste homolog 2 (EZH2) in HCC cells, suggesting that targeting EZH2 may represent a promising strategy to enhance NK cell homing to HCC [13, 32]. Expectedly, in this study we demonstrate that EZH2 inhibitor tazemetostat (Taz), an FDA-approved drug against refractory lymphoma, significantly upregulates CXCL10 expression in Hepa1-6 cells (Figure S10). In addition, Taz-pretreated Hepa1-6 cells can dramatically recruit murine NK cells in a CXCL10-dependent manner (Figure S11). Consistently, Taz treatment substantially increases NK cell infiltration in recurrent HCC

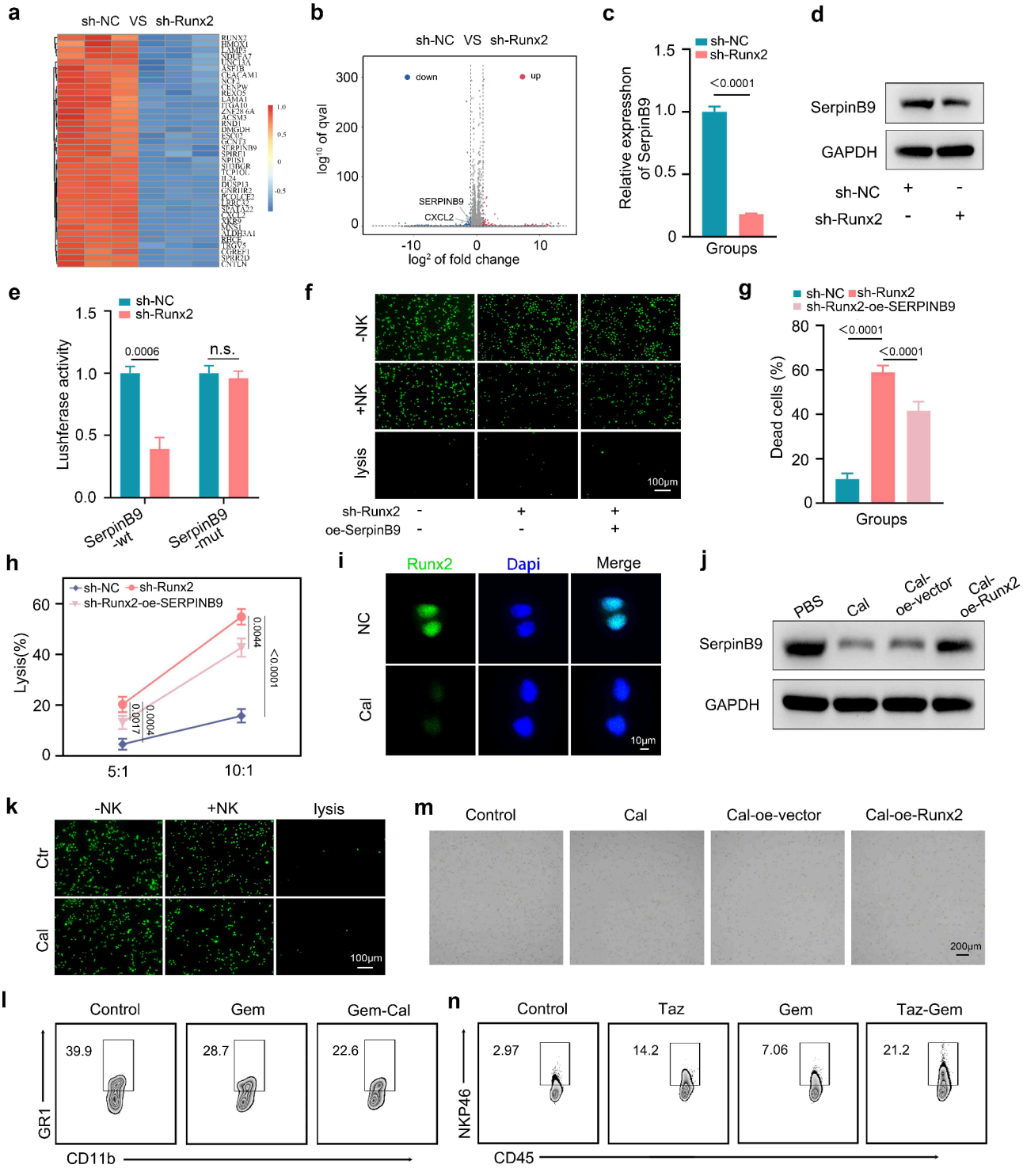

Fig. 3 (See legend on next page.)

(See figure on previous page.)

Fig. 3 Calcitriol reverses the resistance of EpCAM^{high} LCSCs to NK cell-meditated cell lysis. **a-b**: The comparison of mRNA profiles in sh-NC-EpCAM^{high} Huh-7 cells and sh-Runx2-EpCAM^{high} Huh-7 cells through high-throughput sequencing. $n = 3$. **c**: PCR analysis of SerpinB9 expression in sh-NC-EpCAM^{high} Huh-7 cells and sh-Runx2-EpCAM^{high} Huh-7 cells. $n = 3$. **d**: Western blot analysis of SerpinB9 expression in sh-NC-EpCAM^{high} Huh-7 cells and sh-Runx2-EpCAM^{high} Huh-7 cells. **e**: Luciferase reporter assay indicates the binding of Runx2 to the SerpinB9 promoters. $n = 3$. **f**: Calcein AM cytotoxicity assay shows that Runx2 promotes the resistance of EpCAM^{high} Huh-7 cells to NK cell-meditated cell lysis in a SerpinB9-dependent manner. **g**: Quantitative analysis of results in (**f**). $n = 3$. h: LDH cytotoxicity assay shows that Runx2 maintains the resistance of EpCAM^{high} Huh-7 cells to NK cell-meditated lysis in a SerpinB9-dependent manner. $n = 3$. **i**: Immunofluorescence staining of Runx2 in Cal-treated EpCAM^{high} Huh-7 cells and PBS-treated cells. **j**: Western blot analysis of SerpinB9 expression in PBS-treated EpCAM^{high} Huh-7 cells, Cal-treated cells, Cal-treated cells transfected with empty vector, or Cal-treated cells transfected with Runx2-overexpression vector. $n = 3$. **k**: Calcein AM cytotoxicity assay shows that Calcitriol pretreatment reverses EpCAM^{high} Huh-7 cell resistance to NK cell-meditated lysis. **l**: Flow cytometry analysis of intratumoral MDSCs in orthotopic Hepa1-6-HCC murine models in control, Gem treatment, or Gem-Cal treatment groups. $n = 3$. **m**: Representative images of MDSCs attracted by PBS-treated EpCAM^{high} Hepa1-6 cells, Cal-treated cells, Cal-treated cells transfected with empty vector, and Cal-treated cells transfected with Runx2-overexpression vector. **n**: Flow cytometry analysis of intratumoral NK cells in orthotopic Hepa1-6-HCC murine models in control, Taz treatment, Gem, or Taz-Gem treatment groups. Data shown as means ± SD. P values of c were calculated using a two-sided unpaired Student's t test. P values of e, g and h were calculated using a One-way repeated measures ANOVA test

(Fig. 3n & Figure S12). The cGAS-STING pathway activation initiated by cytoplasmic double-stranded DNA (dsDNA) has emerged as a next-generation immunotherapy target. Intriguingly, evidence reveals that cGAS-STING pathway activation can transcriptionally promote CXCL10 expression in tumor cells [33]. In brief, cytosolic dsDNA during DNA damage is first recognized by cGAS protein, which sequentially activates STING/TANK-binding kinase 1 (TBK1)/IFN regulatory factor 3 (IRF3) protein in tumor cells [34]. Then, activated IRF3 binds to the CXCL10 promoter to activate CXCL10 expression as a transcription factor. Notably, it has been revealed that Gem, a DNA damage-inducing chemotherapeutic drug, can activate cGAS-STING pathway in cancer cells [14]. In line with this fact, our γ-H2AX immunofluorescence and PicoGreen assays show that Gem can significantly induce DNA damage and cytosolic dsDNA formation in Hepa1-6 cells (Figure S13). Meanwhile, Gem treatment markedly increases phosphorylation of STING, TBK1, and IRF3, indicating its ability to activate cGAS-STING pathway (Figure S14). Moreover, Taz and Gem can synergistically promote Hepa1-6 cells to express CXCL10 (Figure S10). In consideration of these clues, we further explored whether Taz and Gem can cooperate to enhance NK cell homing to HCC. The gating strategy for identifying murine NK cells is described in Figure S7b. As presented in Figure S11, Hepa1-6 cells treated by Taz and Gem exhibit a more robust capacity of recruiting NK cells than Taz or Gem-treated cells. Consistent with the in vitro results, Taz and Gem can cooperatively elevate NK cell infiltration in recurrent orthotopic Hepa1-6-establishing HCC (Fig. 3n). Therefore, combination of Taz and Gem has great potential of enhancing NK cell homing to HCC.

Preparation and characterization of CGT@POZ powder and its derived hydrogel

As described above, ANKCT combined with a cocktail of Cal, Gem, and Taz may be a brightening strategy to prevent HCC recurrence postresection. Although multidrug combination therapy may improve therapeutic efficacy, it is challenged with limited intratumoral accumulation of drugs and off-target toxicities. To address these challenges, herein we develop a novel nanocomposite self-gelling powder for liver-localized sustained delivery of Cal, Gem, and Taz. In detail, zeolitic imidazolate framework-8 (ZIF-8) nanoparticles are first prepared with reference to the previously reported protocol [35]. The transmission electron microscopy identifies a uniform cubic shape with truncated angle and smooth surface of ZIF-8 nanoparticles (Fig. 4a). The Malvern Nano Zetasizer analysis reveals that these nanoparticles have a diameter of 150 ~ 250 nm (Figure S15). The powder X-ray diffraction (PXRD) analysis indicates that ZIF-8 nanoparticles possess typical crystalline structure (Figure S16). Then, we loaded Cal, Gem, and Taz to ZIF-8 nanoparticles via the impregnation method [36]. The loading efficiencies for Cal, Gem, and Ent are as high as 20.6%, 27.76%, and 23.57%, respectively (Fig. 4b). Next, we prepared OCS via CS oxidization driven by sodium periodate as previously described [19]. Fourier transform infrared (FTIR) analysis of OCS reveals a new infrared band at 1716 cm^{-1} in the spectrum of CS after oxidation treatment (Fig. 4c), which may result from the stretching vibration of aldehyde groups and validates the successful oxidization of CS. The PAAm hydrogel was synthesized by mixing AAm and ammonium persulfate in deionized water solutions and heating the mixture in water bath (70℃, 30 min). Last, we mixed and ground freeze-dried PAAm hydrogel, OCS, and ZIF-8 nanoparticles loaded with Cal, Gem, and Taz to obtain a nanocomposite powder, thereafter termed as CGT@POZ powder. Movie S1 shows that this powder can shortly form hydrogel in situ once contacting water at 37 °C. After dropping anticoagulated blood into CGT@POZ powder deposited in the pentagram mold, a five-pointed bulk hydrogel was also generated (Fig. 4f). Then, FTIR spectra of PAAm, OCS, ZIF-8 nanoparticles, and CGT@POZ hydrogel were compared. The disappearance of characteristic peaks at 1652 cm^{-1} and 1730 cm^{-1} in FTIR spectrum of CGT@POZ hydrogel, which are related to the free amino group in PAAm and the aldehyde group in OCS, respectively,

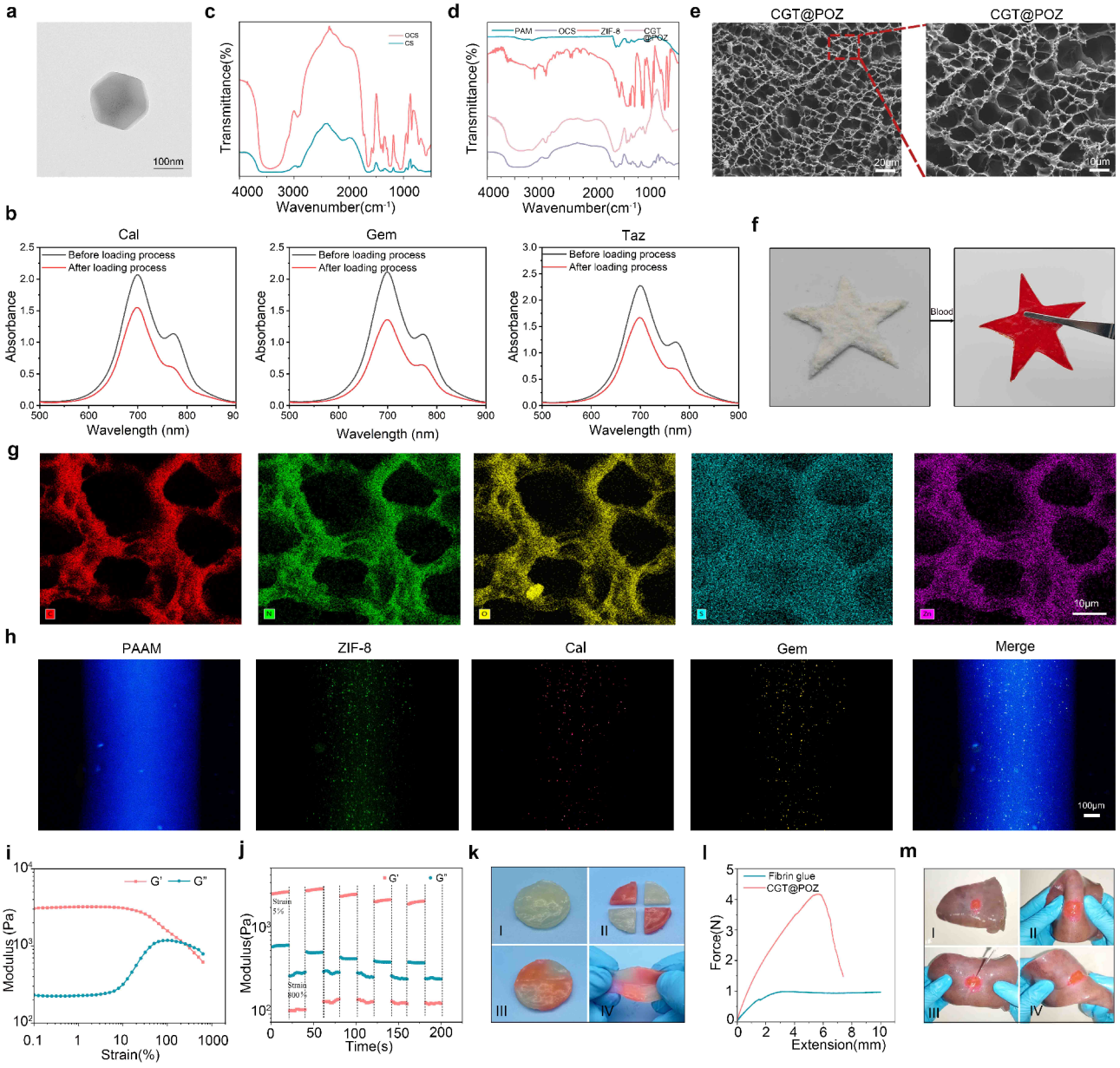

Fig. 4 The preparation and characterization of CGT@POZ powder-derived hydrogel. **a**: The transmission electron microscopy image of ZIF-8 nanoparticles. **b**: The drug-loading efficiency of ZIF-8 nanoparticles. The loading efficiencies of calcitriol, gemcitabine, and tazemetostat are as high as 20.6%, 27.76%, and 23.57%, respectively. **d**: Fourier transform infrared (FTIR) analysis of OCS. **c**: FTIR analysis of CGT@POZ hydrogel. **e**: The scanning electron microscopy image of CGT@POZ hydrogel. **f**: Dropping anticoagulated blood into CGT@POZ powder deposited in the pentagram mold generates a five-pointed bulk hydrogel. **g**: The element mapping analysis of CGT@POZ hydrogel. **h**: Confocal scanning analysis of calcitriol and gemcitabine in CGT@POZ hydrogel. **i**: The strain amplitude sweep test of CGT@POZ hydrogel at an unchanged angular velocity (1 rad s^{-1}) and a temperature of 37 °C. **j**: The continuous cyclic strain test of CGT@POZ hydrogel. **k**: Macroscopic self-healing test of CGT@POZ hydrogel. **l**: Lap shear tests of CGT@POZ hydrogel and fibrin glue. **m**: Macroscopic tissue adhesion test of CGT@POZ hydrogel. Data of k shown as means ± SD

is observed (Fig. 4d). This result indicates that the free amino group in PAAm and the aldehyde group in OCS react into the Schiff's base bond, which can drive the self-gelling of CGT@POZ powder. Besides, the reaction between the amino groups in PAAm and the hydroxyl groups in OCS is able to yield the hydrogen bond, which also contributes to the self-gelation of CGT@POZ powder. By scanning electron microscopy, we observed that CGT@POZ hydrogel exhibits a morphology of homogeneously porous structure (Fig. 4e). The element mapping analysis shows that C, N, S, O, and Zn elements exist in the hydrogel and line around the micropores (Fig. 4g), validating the composition and porous structure of CGT@POZ hydrogel. Moreover, Cal, Gem, and Taz in

ZIF-8 nanoparticles are distributed evenly in the hydrogel (Fig. 4h & Figure S17).

The covalent Schiff's base and hydrogen bonds can endow the hydrogels with powerful self-mending ability, by which the hydrogels can maintain structural integrity to preserve their complex functions in vivo when confronted with external mechanical stresses [5]. To explore the self-healing potential of CGT@POZ hydrogel, the strain amplitude sweep test was first implemented at a fixed angular frequency (10 rad·s^{-1}) at 37 °C. As shown in Fig. 4i, the G′ and G″ values of CGT@POZ hydrogel keeps nearly unchanged until the strain attains ≈ 100%, indicating the gel is capable of sustaining relatively large elastic deformation. Nevertheless, when the strain is further elevated, the G′ and G″ moduli gradually decline and increase, respectively, being equal at ≈ 750% strain, suggesting that the hydrogel may break into a solution state when the strain exceeds this value. Next, we assessed the recoverability of CGT@POZ hydrogel by continuous cyclic strain test (5% strain → 800% strain → 5% strain) at a steady angular frequency (10 rad·s^{-1}). Figure 4j shows that CGT@POZ hydrogel is transformed into a solution state (G′ < G″) at an 800% strain over the critical strain. As soon as the strain declines to 5%, the G′ and G″ values shortly recover to their original values almost without any loss, which indicates that the solution state turns into the hydrogel state again. Thereafter, the macroscopic self-healing test was carried out to further evaluate the self-healing performance of CGT@POZ hydrogel. Figure 4k shows that the hydrogel cut into four pieces self-heals into a single entity under 37 °C for 5 min without any stimulus. Totally, these data verify that CGT@POZ hydrogel exhibits excellent self-healing performance.

The wet tissue adhesion is also a requisite property for biomaterials applied to surgical wound sites. The aldehyde groups in the gels are able to react with the amino groups on wet tissues to generate the Schiff's base bond, resultantly creating a secure interfacial linkage to promote the firm adherence of the hydrogel to wet tissues. To evaluate the wet tissue adhesion capacity of CGT@POZ hydrogel, the lap shear test was first performed. Figure 4l & Figure S18a shows that the hydrogel has a much stronger adhesive strength than fibrin glue. Then, the burst pressure test was performed to further assess the adhesion potency of CGT@POZ hydrogel. In brief, CGT@POZ powder was first deposited onto the surface of fresh porcine skin tissues via a 2 mm diameter cavity in a chamber, where it formed hydrogel in situ (Figure S18b), and subsequently PBS was pumped into the chamber, until the hydrogel failed to withstand the bursting pressure. Similar to the result of the lap shear test, CGT@POZ hydrogel has a much higher burst pressure that fibrin glue (Figure S18c), indicating its great underlying ability to hamper the leakage of blood vessels. In addition, we dropped water to CGT@POZ powder deposited onto the surface of fresh porcine liver to generate the hydrogel in situ, and then the hydrogel was twisted, bended and flushed the hydrogel using water to evaluate its tissue adhesion ability. As shown in Fig. 4m, the hydrogel is firmly adhered to the porcine liver regardless of repeated twisting, bending, and flushing. These results indicate that CGT@POZ hydrogel owns powerful wet tissue adhesion capacity.

Biocompatibility, biodegradability, and drug release of CGT@POZ hydrogel

To assess the biocompatibility of CGT@POZ hydrogel in vitro, the hemolysis experiment was first conducted. As presented in Figure S19, the solution turned red in the Triton group, but it was nearly clear in the hydrogel and PBS groups. The hemolysis ratios in the hydrogel group and PBS group were significantly lower than 5%, which has been proposed as the threshold of acceptable hemocompatibility in vitro. Then, we cultured THLE-2 cells in 24-well plate coated with or without CGT@POZ hydrogel, which were subsequently subjected to live/dead staining assay. Figure 5a-b shows that CGT@POZ hydrogel only caused subtle toxicity to THLE-2 cells with over 85% of cells viable after 24 h and 48 h incubation. These results indicate that the gel has favorable biocompatibility in vitro. To assess the biocompatibility in vivo, we performed liver resection on a total of 10 mice and then categorized those mice into 2 groups randomly: group 1 for applying CGT@POZ powder to liver resection margin and group 2 for no treatments. At the indicated time points after treatment, blood samples were gathered from mice for biochemical examination and hemogram analysis. The results showed that this powder did not markedly affect alanine aminotransferase (ALT), aspartate aminotransferase (AST), alkaline phosphatase (ALP), and blood urea nitrogen (BUN) at the indicated time points, indicating no obvious harm to renal and hepatic functions (Fig. 5c). Either, CGT@POZ powder had no significant influence on red blood cell (RBC) count, white blood cell (WBC) count, plateletcrit (PCT), and red cell distribution width (RDW) (Fig. 5d). In addition, we also collected liver, kidney, heart, spleen, and lung tissue samples from mice and subjected them to histopathological analysis. As displayed in Fig. 5e, CGT@POZ powder caused no significant tissue damage to any organ. Moreover, we did not observe obvious increase of cytokine storm-associated cytokines including IL-6, IL-17 A, and IL-5 after CGT@POZ powder treatment (Figure S20) [37]. In general, these data clarify that CGT@POZ powder own satisfactory biocompatibility.

To evaluate the biodegradability of CGT@POZ hydrogel in vitro, we first immersed it in PBS (pH = 7.4) at

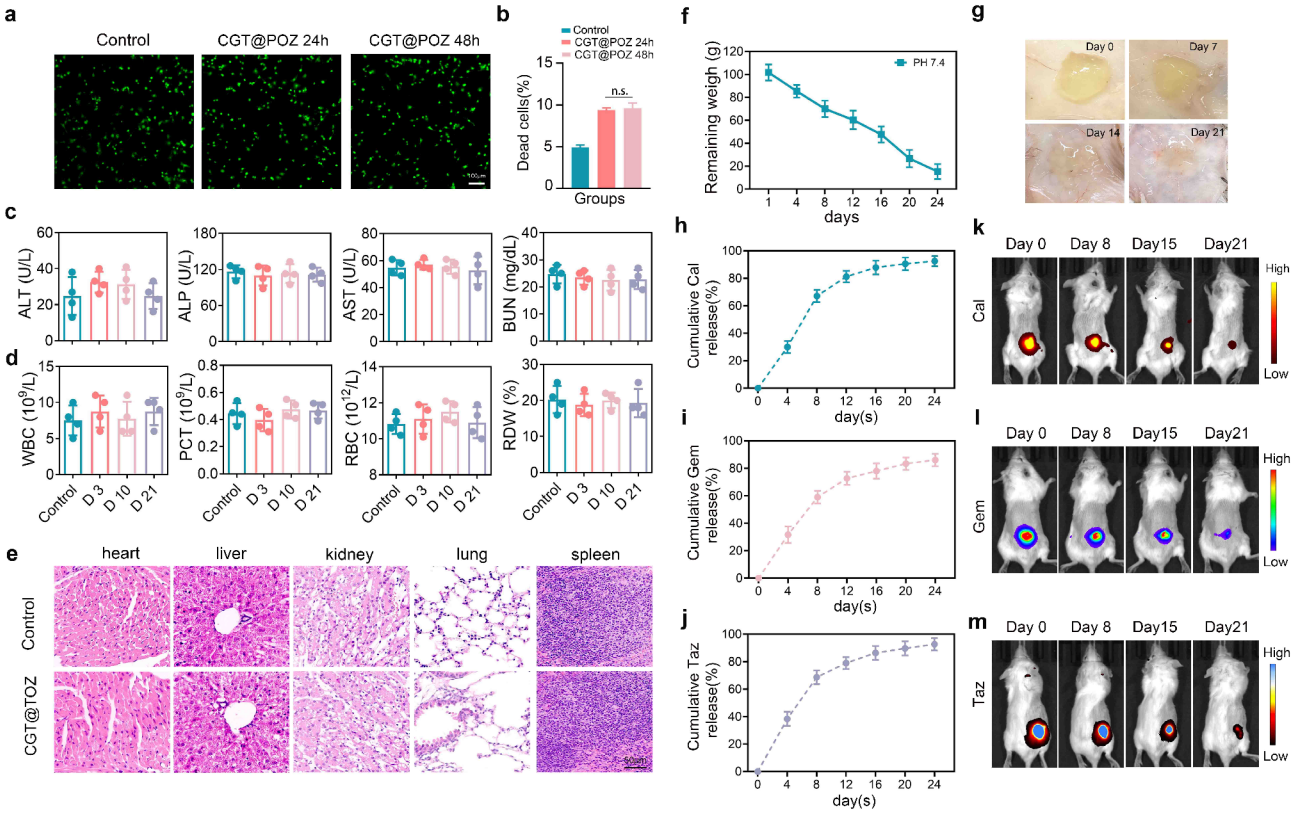

Fig. 5 The biocompatibility of CGT@POZ powder. **a-b**: Live/dead staining of THLE-2 cells in coculture with CGT@POZ powder-formed hydrogel versus untreated cells. **c**: Serum concentrations of alanine aminotransferase (ALT), aspartate aminotransferase (AST), alkaline phosphatase (ALP), and blood urea nitrogen (BUN) in rats of control and CGT@POZ powder treatment groups. **d**: The levels of red blood cell (RBC) count, white blood cell (WBC) count, plateletcrit (PCT), and red cell distribution width (RDW) in mice of control and CGT@POZ powder treatment groups. **e**: HE staining of tissue sections of liver, kidney, heart, spleen, and lung collected from control mice and CGT@POZ powder-treated mice. **f**: The biodegradation behavior of CGT@POZ powder-formed hydrogel in vitro. $n = 3$. **g**: The general observation of CGT@POZ powder-derived hydrogel after being subcutaneously inserted into dorsal region of mice. **h-j**: Accumulative release curves of Cy5.5-labeled Cal, Gem and Taz from CGT@POZ powder-derived hydrogel in vitro. **k-m**: Fluorescence IVIS imaging of Cy5.5-labelled Cal, Gem, or Taz in CGT@POZ powder-derived hydrogel subcutaneously implanted into the back of mice. $n = 3$ mice/group. Data shown as means ± SD

37 °C and weighed its residual bulk at the selected time points. It was found that that there was a gradual decline in the weights of CGT@POZ hydrogel (Fig. 5f). Then, we implanted CGT@POZ hydrogel into mice subcutaneously and made the general observation on the remained hydrogel on day 1, day 7, day 14, and day 21. Figure 5g showed that the hydrogel bulk gradually shrank with a subtle residual on day 21. These results confirm that CGT@POZ hydrogel has a proper biodegradability. To investigate the drug release behavior of CGT@POZ hydrogel, we first labeled Cal, Gem, or Taz with Cy5.5 and then loaded them to ZIF-8 nanoparticles, which were mixed and ground with freeze-dried PAAm hydrogel and OCS to produce CGT@POZ powder. Next, we prepared CGT@POZ hydrogel by adding PBS into this powder and immersed them in pH 7.4 PBS. Subsequently, the supernatants at the predetermined intervals were collected for measuring the released drug concentration using the UV-Vis-NIR absorbance spectrum. As illustrated in Fig. 5h-j, the hydrogel allows a sustained drug release in vitro. After immersion for 24 days, the cumulative release rates of the hydrogel for Cal, Gem, or Taz were 92. 5%, 86%, and 92.7%, respectively. To evaluate the drug release in vivo, we implanted the hydrogel loading Cy5.5-labeled drugs into mice subcutaneously and monitored the residual drugs dynamically using the bioluminescence imaging system. Figure 5k-m shows that the fluorescence signals of Cy5.5 gradually fades and are nearly undetectable on 21 day. To further assess the controlled release of Cal, Gem, and Taz specifically within liver, we first applied Cy5.5-labelled CGT@POZ powder to liver resection margin of HCC-bearing mice. Next, the liver tissues were harvested from mice on 1 day, 7 day, 14 day and 21 day after treatment for preparing the frozen slices. Then, the signal from Cy5.5-labelled drugs in those frozen slices were analyzed using confocal laser scanning microscope (Leica). As presented in Figure S21, CGT@POZ powder allowed for a gradual release of Cal, Gem, and Taz specifically within liver, but not in other organs including heart, spleen, lung, and kidney. In general,

these results indicate that CGT@POZ hydrogel can yield a sustained liver-localized drug release after its application to liver resection bed.

Hemostasis effect of CGT@POZ powder

The massive hemorrhage can cause a series of severe complications, which delays the postoperative recovery and impairs the life quality of patients. Moreover, blood loss may increase the risk of postoperative cancer recurrence and metastasis through fostering cancer cells to disseminate into the circulatory system [38]. Liver is an organ with rich blood supply, so liver surgery is usually accompanied with a high risk of massive hemorrhage. In clinical practice, parts of HCC patients suffer liver cirrhosis with impaired coagulation function, which further elevates the inclination of surgical bleeding. To date, enormous efforts have been paid to arrest and prevent excessive blood loss during liver surgery, but it still remains a critical concern in individual patients, particularly those undergoing major hepatectomy. Growing studies have shown that the hydrogels can be engineered to possess hemostasis performance, in addition to drug delivery. As demonstrated above, CGT@POZ hydrogel has strong wet tissue adhesion ability, which may help to effective hemostasis through forming physical barriers to seal bleeding sites. The aggregation of red blood cells at bleeding sites also represents an essential event supporting hemostasis. Interestingly, CGT@POZ powder immersed in whole blood can significantly aggregate red blood cells versus fibrin glue (Figure S22). Therefore, we further cut the tail or the femoral artery, and punctured the heart of rats to establish acute bleeding models, and evaluated the hemostatic effect of CGT@POZ powder in these models. As expected, we observed that the application of CGT@POZ powder to wound sites could cease bleeding around 5 s without rebleeding after 3 min (Fig. 6a-c & Movie S2-4). Then, we further evaluated the capability of CGT@POZ powder to resist massive hemorrhage by creating the wounds with 2 cm of length and 1 cm of depth in the spleen and liver of porcine, respectively (Fig. 6d). As presented in Fig. 6e-f & Movie S5-8, depositing 200 mg of CGT@POZ powder to the bleeding sites of spleen and liver generates a complete hemostasis 3 min after treatment, whereas the deposition of 500 mg of commercial chitosan powder fails to stop bleeding, suggesting that CGT@POZ powder may also be used to arrest hemorrhage in liver surgery. Currently, minimally invasive surgery is preferentially selected to implement hepatectomy for HCC, unless absolute contraindications exist. Accordingly, we further assessed the utility of CGT@POZ powder in minimally invasive surgery using a rabbit model. Figure S23 shows that CGT@POZ powder can be smoothly spread to the injured sites of liver via laparoscopic approach. Altogether, CGT@POZ powder can be used to stop bleeding during liver surgery in the context of open operation and minimally invasive surgery.

Liver-localized CGT@POZ powder treatment reinvigorates NK cell antitumor immunity to prevent HCC recurrence

To explore whether CGT@POZ powder treatment can effectively prevent HCC recurrence, we first prepared POZ powder without drugs (POZ), POZ powder loaded with Cal (C@POZ), POZ powder loaded with Gem (G@POZ), POZ powder loaded with Taz (T@POZ), POZ powder loaded with Cal and Gem (CG@POZ), POZ powder loaded with Gem, and Taz (GT@POZ), POZ powder loaded with Cal and Taz (CT@POZ), and POZ powder loaded with Cal, Gem, and Taz (CGT@POZ). Thereafter, we established orthotopic Hepa1-6 tumor-bearing models in a total of 60 Balb/c mice, performed liver resection on these mice, and then randomized them into 10 groups (Fig. 7a): group 1 for applying chitosan powder to liver resection margin (G1, Control), group 2 for applying POZ powder (G2, POZ), group 3 for applying C@POZ powder (G3, C@POZ), group 4 for applying G@POZ powder (G4, G@POZ), group 5 for applying T@POZ powder (G5, T@POZ), group 6 for applying CG@POZ powder (G6, CG@POZ), group 7 for applying GT@POZ powder (G7, GT@POZ), group 8 for applying CT@POZ powder (G8, CT@POZ), group 9 for intravenous injection of Cal, Gem, and Taz (G9, CGT-iv), and group 10 for applying CGT@POZ powder (G10, CGT@POZ). The tumor recurrence in each group was dynamically monitored through using a fluorescence imaging system. As displayed in Fig. 7b-d, POZ, C@POZ, and CGT-iv treatments had no significant effects on the incidence of tumor recurrence compared to control group, while other treatments could not only reduce tumor recurrence incidence, but also delay the growth of recurrent tumor. Particularly, CG@POZ powder treatment performed best in this regard among all the treatments. It should be emphasized that CGT-iv treatment exerted no significant on HCC recurrence, which may result from the low dosage and poor bioavailability of Cal, Gem, and Taz. The remarkable advantage of CGT@POZ treatment over CGT-iv treatment in preventing HCC recurrence strongly supports that our newly developed drug delivery platform possesses great potential of clinical translation. Apart from effective control on HCC recurrence, the survival prognosis of mice was also largely improved by CGT@POZ treatment (Fig. 7e). The body weight of mice in all groups dropped at day 10 significantly, which may be mainly attributed to the removal of tumor mass, blood loss, and the evaporation of peritoneal fluid (Fig. 7f). The continuous decline of body weight in control and POZ groups was observed, which may result from surgical stress and tumor-related cachexia. Remarkably, no significant drop of body weight

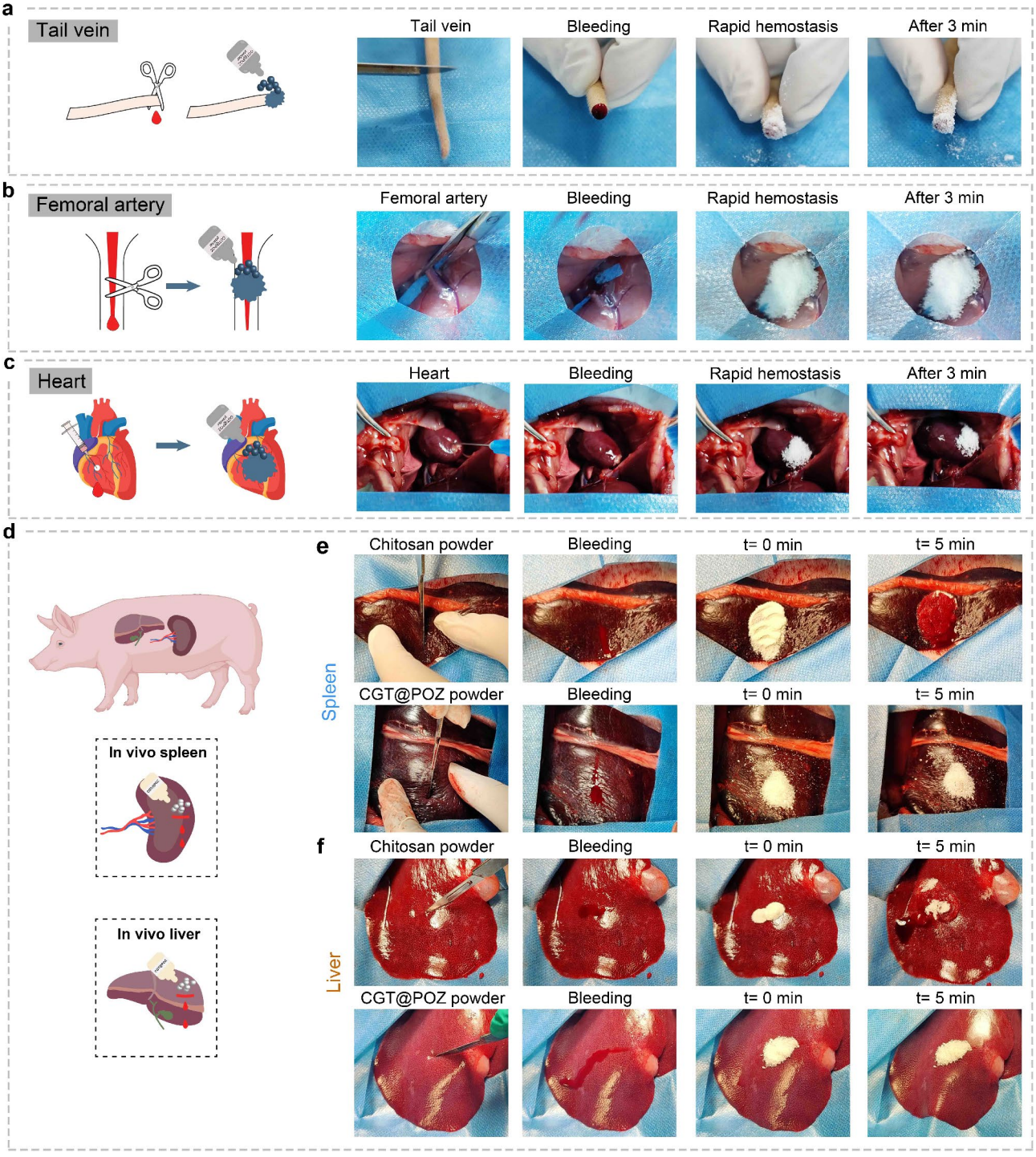

Fig. 6 Hemostasis performance of CGT@POZ powder in rat and porcine models. **a-c**: The schematics and images of inducing acute bleeding and ceasing bleeding through applying different hemostatic materials in tail vein (**a**), femoral artery (**b**) and heart (**c**) of rats. $n = 3$. **d**: The schematics of inducing massive bleeding and stopping bleeding through applying different hemostatic materials in porcine spleen and liver. **e**-**f**: Images of live porcine spleen (**e**) and liver (**f**) before and after applying distinct hemostatic materials. $n = 3$

was observed in POZ group compared to control group, further supporting that our designed powder has good biocompatibility. Therefore, these findings demonstrated that liver-localized treatment by CGT@POZ powder can effectively prevent HCC recurrence postresection without systemic toxicity.

To determine whether NK cell antitumor immunity is implicated in CGT@POZ powder-mediated inhibition

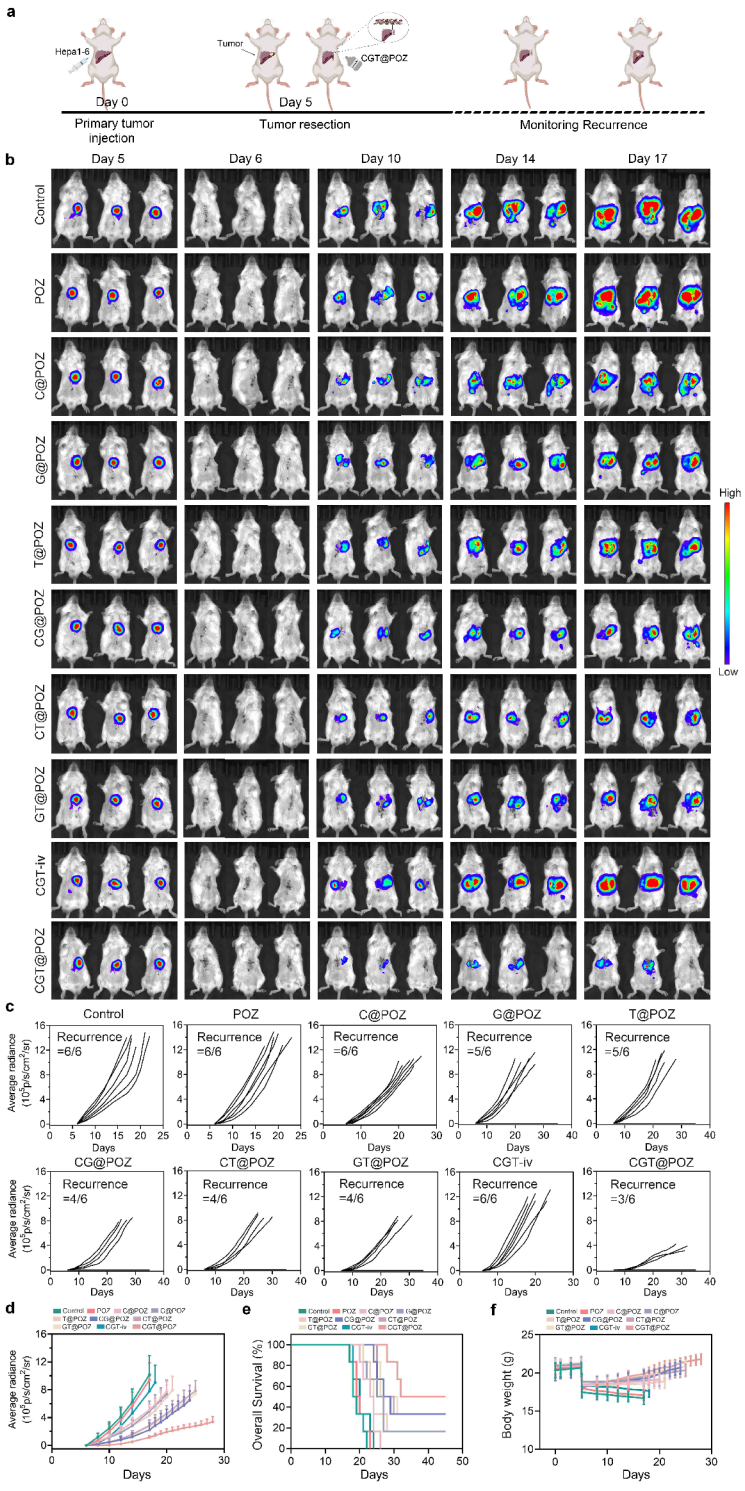

Fig. 7 Surgical margin-localized application of CGT@POZ powder prevents HCC recurrence postresection. a: Schematic diagram of CGT@POZ powder treatment for preventing postoperative tumor recurrence in Hepa1-6 cell-HCC murine models. b. Imaging of recurrent HCC using the bioluminescence technique. c. The rates of HCC recurrence in mice treated with distinct modalities. d: Survival prognosis of mice in different treatment groups. e: Average tumor regrowth kinetics in mice in different treatment groups. f: Dynamic weights of mice in different groups. $n = 6$. Data shown as means ± SD. P values of d and f were calculated using a One-way repeated measures ANOVA test. P values of e was performed by the Kaplan-Meier analysis

on HCC recurrence, we first created orthotopic Hepa1-6 tumor-bearing models in 60 Balb/c mice and performed partial liver resection on these mice to remove primary tumors. These mice were then randomized into 10 groups as described above. 7 days after treatment, the recurrent tumors from mice in each group were collected for the flow cytometry analysis of percentages of MDSCs, NK cells, $GZMB^+$ NK cells and TNF-γ^+ NK cells (Fig. 8a). MDSCs are essential immunosuppressive cells in the TME of HCC, which can not only directly inhibit NK cell cytotoxicity, but also induce NK cell dysfunction by boosting the expansion and recruitment of other immunosuppressive cells [8]. In addition, evidence reveals that hepatectomy-induced stress is able to expand MDSCs largely in HCC patients [9]. Moreover, NK cell infusion itself can drive MDSC recruitment into HCC [10]. Thus, these evidences indicate that MDSCs may occupy a dominant position in immunosuppressive immune cell-meditated NK cell dysfunction in the context of hepatectomy. As we demonstrated above, Cal and Gem synergistically reduced the infiltration of MDSCs in orthotopic murine HCC (Fig. 3l). Expectedly, it was observed that C@POZ and G@POZ powder treatment could decrease the percentage of MDSCs in recurrent HCC compared to control treatment and POZ treatment (Fig. 8b). Moreover, CG@POZ powder and CGT@POZ powder performed much better in this regard than C@POZ and G@POZ powder (Fig. 8b-c). Although unselective EZH2 inhibition can exert significant antitumor immunity in a multiple of cancers including HCC, it directs myeloid differentiation from primitive hematopoietic progenitor cells to increase the percentage of tumor-infiltrating MDSCs, resultantly limiting therapeutic efficacy, implying the rationale of combining EZH2 inhibitor and strategies targeting MDSCs for treating cancers [39]. Consistently, our data showed that there was a higher percentage of MDSCs in recurrent HCC of T@POZ group than control group. Of note, the percentages of tumor-infiltrating MDSCs in CG@POZ and CGT@POZ powder groups have no significant differences, indicating that Cal and Gem can effectively offset Taz-induced myeloid differentiation from primitive hematopoietic progenitor cells. In addition to TME-mediated suppression on NK cell function, insufficiency of NK cell homing to tumor sites also severely limits ANKCT efficacy in cancer [40–42]. Notably, our data mentioned above proves that Taz and Gem can synergistically promote HCC cells to express and release NK cell chemokine CXCL10, thereby boosting NK cell homing to HCC (Figure S8 & Fig. 3n). Consistently, T@POZ and G@POZ powder treatment significantly increased NK cell percentage in recurrent HCC versus control treatment and POZ treatment (Fig. 8d-e). Moreover, GT@POZ powder treatment was much superior to T@POZ and G@POZ powder treatment in driving NK cell homing to HCC. Interestingly, CGT@POZ powder treatment also had a stronger ability to increase NK cell percentage in HCC than GT@POZ powder treatment. Evidence reveals that Cal can induce DNA damage in tumor cells, and perhaps could activate cGAS-STING pathway to upregulate NK cell chemokine CXCL10 [43, 44], which may partly explain the advantage of CGT@POZ powder treatment in increasing NK cell percentage in HCC over GT@POZ powder treatment. Moreover, we found that the percentage of $GZMB^+$ and TNF-γ^+ NK cells in CGT@POZ group was highest among all groups (Fig. 8f-i). Altogether, these results suggest that CGT@POZ powder treatment can enhance NK cell antitumor immunity through relieving TME-mediated inhibition on NK cell function and boosting NK cell homing to HCC, which at least partly accounts for its effect in preventing HCC recurrence postresection.

Liver-localized CGT@POZ powder treatment improves adoptive NK cell therapy efficacy in HCC

To explore whether CGT@POZ powder treatment sensitizes ANKCT to thwart postsurgical HCC recurrence, we first used Hepa1-6 cells to establish orthotopic HCC recurrence models in 30 Balb/c mice as described above (Fig. 9a). Then, these mice were randomly divided into 3 groups: group 1 for no additional treatments (Control), group 2 for allogenic NK cell infusion (NK), and group 3 for applying CGT@POZ powder to surgical margin followed by allogenic NK cell infusion (CGT@POZ-NK). The tumor recurrence in was dynamically tracked using a fluorescence imaging system. Figure 9b-d shows that NK cell infusion delayed recurrent HCC growth and extended survival time to an extent, but failed to lower the incidence of HCC recurrence postresection. Of note, NK cell infusion combined with CGT@POZ powder not only inhibited recurrent HCC growth, but also significantly reduced postoperative tumor incidence. These results demonstrate that liver-localized CGT@POZ powder treatment can sensitize ANKCT to combat postsurgical HCC recurrence.

The modification of NK cells with chimeric antigen receptors (CAR) also represents a bright strategy to improve ANCT efficacy. To date, CAR-modified NK (CAR-NK) cells have been observed to yield encouraging benefits in many preclinical and clinical studies of solid tumors [45]. NK-92 cell line, established from a 50-year-old male patient struggled with progressive non-Hodgkin's lymphoma, has been widely used as a cancer therapeutic cell. NK-92 cells have been modified to express CARs against multiple tumor targets, such as EGFR, Her2, and EpCAM. These CAR-NK-92 cells display more selective and robust ability to kill tumor cells than unmodified NK-92 cells. Similar to infused unmodified NK cells, CAR-NK cell antitumor function is also

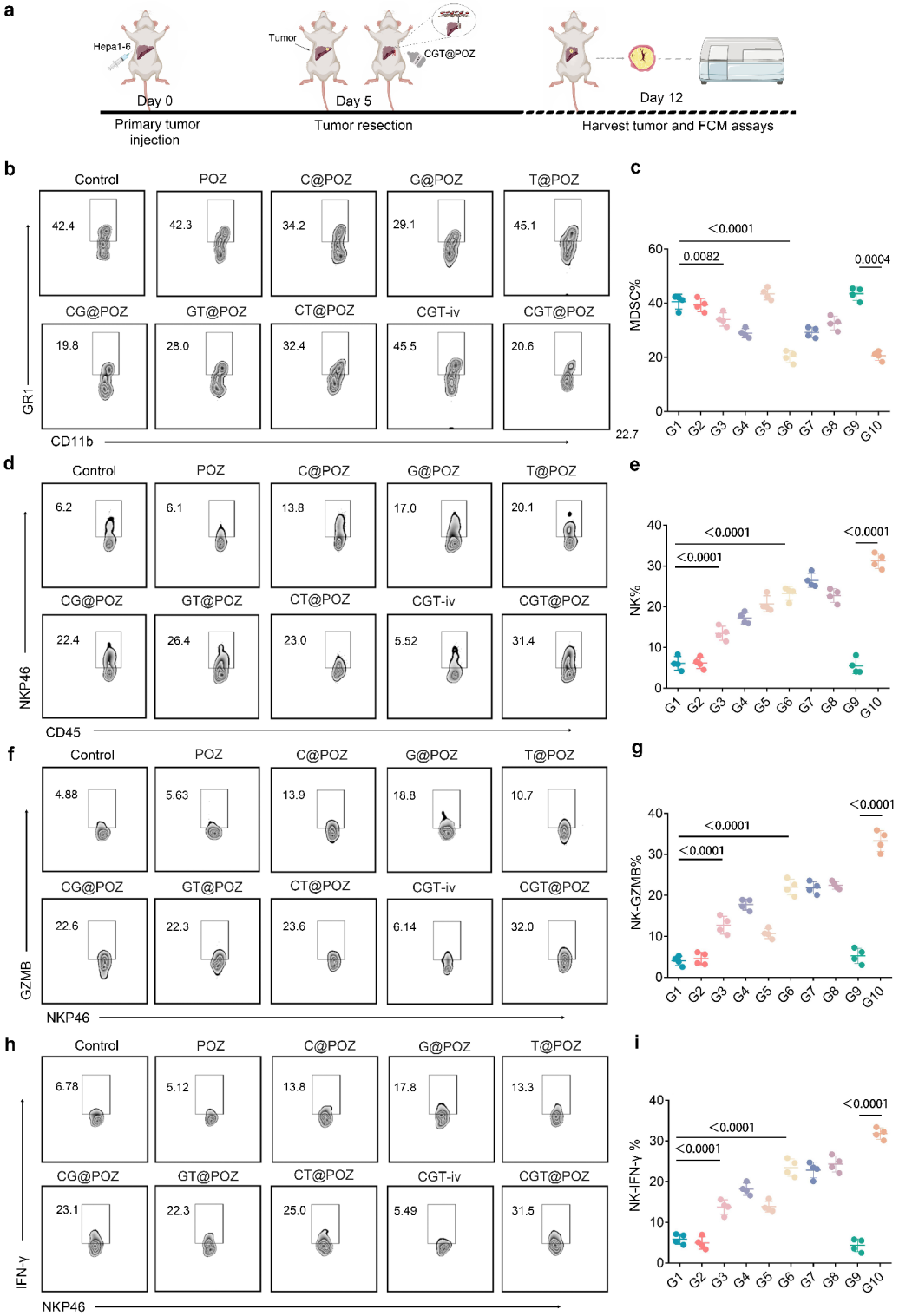

Fig. 8 Surgical margin-localized treatment of CGT@POZ powder improves NK cell antitumor immunity in recurrent HCC foci. **a**: Schematic diagram of flow cytometric analysis of immune cells infiltrated in recurrent HCC foci. After seven days of surgery, the recurrent tumors were gathered and subjected to flow cytometric analysis of immune cells. **b**-**c**: Intratumoral percentage of $CD11b^{+}Gr1^{+}$MDSCs. **d**-**e**: Intratumoral percentage of $CD45^{+}NKP46^{+}$ NK cells. **f**-**g**: Intratumoral percentage of $NKP46^{+}$ $GZMB^{+}$ NK cells. **h**-**i**: Intratumoral percentage of $NKP46^{+}$ IFN-γ^{+} NK cells. Data were shown as means ± SD. P values of **c**, **e**, **g**, and **i** were calculated using a One-way repeated measures ANOVA test

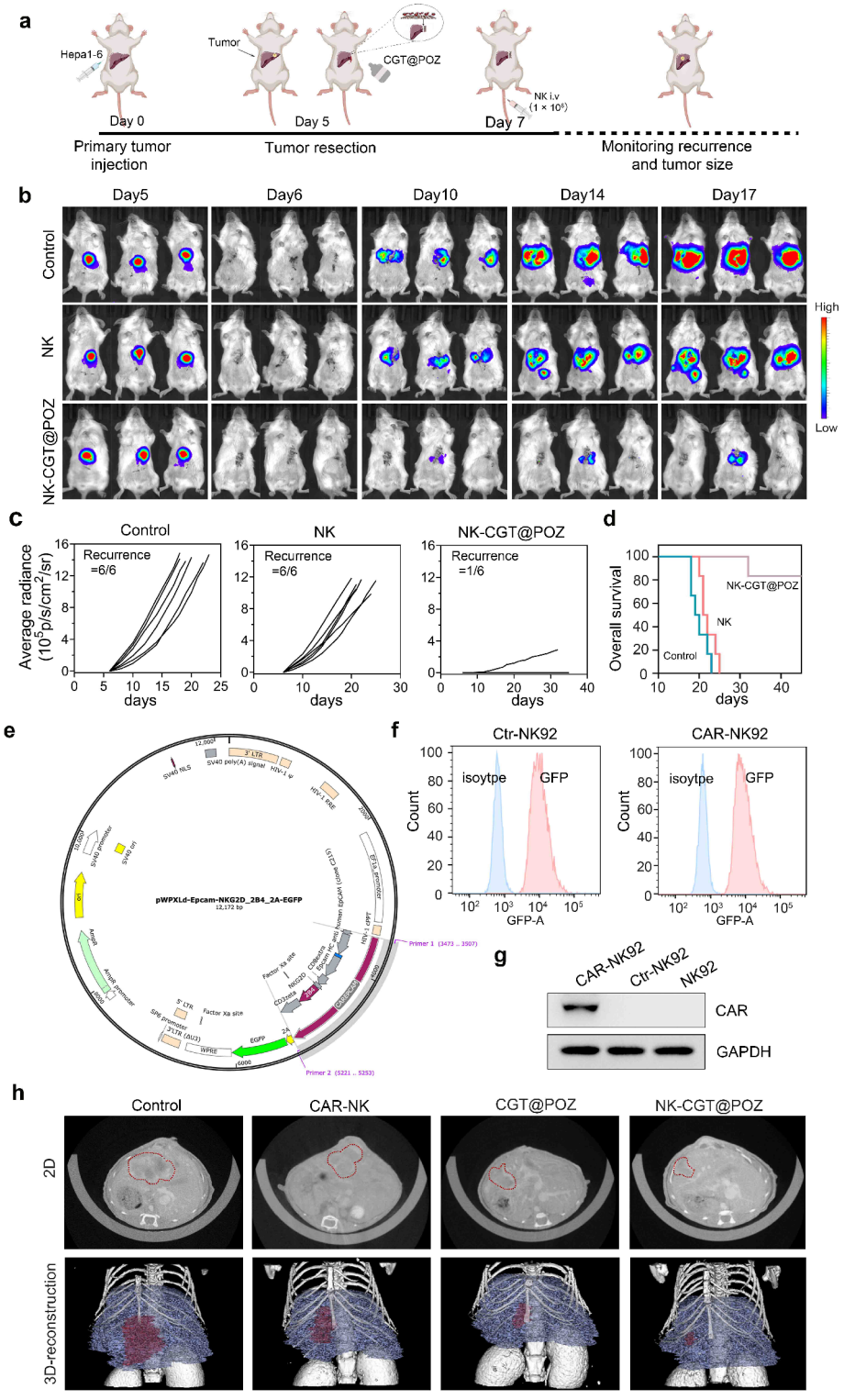

Fig. 9 Liver-localized CGT@POZ powder treatment sensitizes adoptive NK cell therapy to curb HCC recurrence. **a**: The schematic diagram of adoptive allogenic NK cell therapy combined with CGT@POZ powder for preventing postsurgical tumor recurrence in orthotopic Hepa1-6 tumor-bearing murine models. **b**: The representative bioluminescence imaging of recurrent HCC in mice subjected to different therapeutic modalities. **c**: Quantitative analysis of recurrent HCC growth in (**b**). $n = 6$. **d**: Overall survival analysis of mice in different treatment groups. **e**: The schematic illustrating the characterization of EpCAM-specific CAR-NK-92 cells. **f**: Flow cytometry analysis of transduction efficiency of empty lentivirus vector (Ctrl-NK-92) or lentivirus containing the EpCAM-specific CAR encoding sequence (CAR-NK-92) in NK-92 cells. **g**: Western blot analysis of CAR expression in NK-92 cells, CAR-NK-92 cells, and Ctrl-NK-92 cells. **h**: The representative micro-CT images of tumor volumes in HCC PDX immune-humanized murine models in different treatment groups. $n = 5$ mice/group. P values of d was performed by the Kaplan-Meier analysis

challenged with immunosuppressive microenvironment of solid tumors, which appeals for CAR-NK cell-based combination therapy. Therefore, we further determined whether CGT@POZ powder treatment improves EpCAM-CAR-NK-92 cell therapy efficacy in HCC. To achieve this, we first constructed a second-generation CAR, which consists of an EpCAM-specific scFv linked to CD8 hinge and transmembrane domains, followed by the intracellular signaling domains of 4-1BB and CD3ζ in sequence (Fig. 9e). This construct was then inserted into a lentiviral vector system containing sequences encoding green fluorescent protein (GFP). Then, NK-92 cell lines were transduced with EpCAM-specific CAR and empty lentiviral vector to generate EpCAM-CAR-NK-92 and Ctrl-NK-92 cells, respectively. As presented in Fig. 9f-g, the percentages of GFP-positive cells in both CAR- and empty vector-transduced NK-92 cells were around 80%, and EpCAM-CAR was expressed in CAR-transduced NK-92 cells, but not in Ctrl-NK-92 cells. Next, we performed Calcein AM cytotoxicity and LDH release assays to compare EpCAM-CAR-NK-92 and Ctrl-NK-92 cell-mediated cytotoxicity to $EpCAM^{high}$ Huh-7 cells. Figure S24 shows that EpCAM-CAR-NK-92 cells exhibit more robust killing to $EpCAM^{high}$ Huh-7 cells at E: T ratios of 5: 1 and 10: 1 than Ctrl-NK-92 cells. Then, we established orthotopic patient-derived xenograft (PDX) HCC model in a total of 20 immune-humanized NOD scid gamma (NSG) mice (Figure S25). These mice were randomized into 4 groups: group 1 for no treatments (Control), group 2 for unmodified NK-92 cell therapy (NK), group 3 for EpCAM-CAR-NK-92 cell therapy (CAR-NK), and group 4 for applying CGT@POZ powder to tumor surface area and EpCAM-CAR-NK-92 cell therapy (CGT@POZ-CAR-NK). 3 weeks after treatment, the tumor volumes in all groups were examined through micro-computed tomography scanning. As displayed in Fig. 9h & Figure S26, the tumor volumes in NK, CAR-NK, and CGT@POZ-CAR-NK groups were smaller than those in control group and decreased progressively. Altogether, these results demonstrate that liver-localized CGT@POZ powder treatment can also improve EpCAM-CAR-NK cell therapy efficacy in HCC.

Conclusion

In summary, a hemostatic nanocomposite self-gelling powder is synthesized by mixing and grinding freeze-dried PAAm hydrogel, OCS, and ZIF-8 nanoparticles loaded with Cal, Gem, and Taz, which can allow for a sustained liver-localized drug delivery to mitigate TME-mediated immunosuppression and drive NK cell homing to tumor sites, consequently enhancing ANKCT against HCC recurrence post-resection. Several limitations exist in our study, which should be seriously considered. First, ZIF-8 nanoparticles are a sub-family of metal-organic frameworks characterized with a three-dimensional framework in which Zn^{2+} coordinates with 2-methylimidazole, and they have great potential as a platform delivering proteins, nucleic acids, and small-molecule drugs [46]. Therefore, our newly developed powder may also serve as a good deliver platform of other anti-HCC drugs, such as Doxorubicin [47], Norcantharidin [48], Bevacizumab, and Oxaliplatin [49]. This issue should be further explored in future study, which may help to the clinical generalizability of our powder in the context of individualized anti-cancer treatment. Second, we have clarified the rationale of combining Cal, Gem, and Taz to enhance ANKCT against HCC recurrence, but we did not determine what is the optimum concentration of each drug in terms of therapeutic effect, which may also limit the clinical translation of our findings. Last but not least, our work does not provide strategies of scaling CGT@POZ production. There are several challenges in scaling CGT@POZ production. First, variations in polymer synthesis, reagent quality, and reaction conditions may affect the properties of CGT@POZ, such as molecular weight, functionality, and therapeutic efficacy. Therefore, it is of much essence to establish robust quality control system to ensure reproducibility, stability, and purity of scaling production. Second, transitioning from laboratory-scale to industrial-scale production requires optimization of synthetic pathways, purification methods, and solvent usage, which often refers to significant re-engineering for ensuring cost efficiency and scalability without compromising quality. Third, variability in raw material sources can introduce batch-to-batch inconsistencies of mass production, so a consistent and high-quality supply of raw materials should be ensued. In addition, the raw materials, labor, facility upgrades, and compliance costs can make large-scale CGT@POZ powder production economically challenging.

Supplementary Information

The online version contains supplementary material available at https://doi.org/10.1186/s12951-025-03424-9.

Supplementary Material 1
Supplementary Material 2
Supplementary Material 3
Supplementary Material 4
Supplementary Material 5
Supplementary Material 6
Supplementary Material 7
Supplementary Material 8
Supplementary Material 9

Acknowledgements
This work was supported by Cuiying Biomedical Research Center, Lanzhou University Second Hospital.

Author contributions
Yihang Gong, Yusheng Cheng, Xin Li, Fanxin Zeng, and Bo Liu conducted the experiments and analyzed the data. Yihang Gong and Yusheng Cheng wrote and revised the manuscript. Wenjie Chen, Feng Zhang, Haofei Chen, and Weixiong Zhu checked the data and revised the manuscript. Wence Zhou, Tiangen Wu, Lei Zhou, and Hui Li designed and supervised this research.

Funding
This work was funded by the National Natural Science Foundation of China (82303474, 82360550, 82260555), Lanzhou University Second Hospital Talent Introduction Plan (yjrckyqdj-2024-05), Medical Innovation and Development Project of Lanzhou University (lzuyxcx-2022-177), Major Science and Technology Projects of Gansu Province (22ZD6FA021-4), Joint Research Fund General Projects of Gansu Province (23JRRA1508), Cuiying Science and Technology Innovation Project Of The Second Hospital of Lanzhou University (CY2023-YB-A02), China Postdoctoral Science Foundation (2022M720176, 2024T171075), Postdoctoral Fellowship Program of CPSF, the Natural Science Foundation of Guangdong Province (2024A1515010701, 2414050003502, 2019A1515011850, 2022A1515012224), Guangzhou Municipal Science and TechnologyProject (2025A03J3207), Starting Package of Xiang'an Hospital of Xiamen University (XAH23017), Fujian Provincial Natural Science Foundation of China (2024J01013), Beijing Huakang Public Welfare Foundation (LYF20240257), and Beijing Science and Technology Innovation Medical Development Foundation (LYF20240157).

Data availability
No datasets were generated or analysed during the current study.

Declarations

Ethics approval and consent to participate
This study received the approval from the Ethics Review Board of the Third Affiliated Hospital, Sun Yat-sen University (Approval no. II2024-166-01), the Animal Care and Use Committee of Jennio Biotech Co.,Ltd (IACUC-2023-A039), and the Animal Care and Use Committee of Huateng BioScience (C202304-14).

Consent for publication
All authors have approved the manuscript and agree for the submission.

Competing interests
The authors declare no competing interests.

Author details
[1]The Second Clinical Medical School of Lanzhou University, Lanzhou 730000, China
[2]Department of General Surgery, Department of Biotherapy, Lanzhou University Second Hospital, Lanzhou 730000, China
[3]Gansu Province Precision Diagnosis and Treatment Engineering Research Center of Hepatobiliary Pancreatic Diseases, Gansu Province Key Laboratory of Environmental Oncology, Lanzhou 730000, China
[4]Department of Hepatic Surgery and Liver Transplantation Center, Organ Transplantation Institute, Organ Transplantation Research Center of Guangdong Province, Guangdong Province Engineering Laboratory for Transplantation Medicine, The Third Affiliated Hospital of Sun Yat-sen University, Sun Yat-sen University, Guangzhou 510630, China
[5]Guangdong Key Laboratory of Liver Disease Research, the Third Affiliated Hospital of Sun Yat-sen University, Guangzhou 510630, China
[6]Biotherapy Centre & Cell-gene Therapy Translational Medicine Research Centre, The Third Affiliated Hospital, Sun Yat-sen University, Guangzhou 510630, China
[7]Department of Hepatobiliary Pancreatic Tumor Center, Chongqing Key Laboratory of Translational Research for Cancer Metastasis and Individualized Treatment, Chongqing University Cancer Hospital, Chongqing 400030, China
[8]Guangzhou Key Laboratory of Spine Disease Prevention and Treatment, Department of Orthopaedic Surgery, The Third Affiliated Hospital of Guangzhou Medical University, Guangzhou 510150, China
[9]Department of Hepatobiliary & Pancreatic Surgery, Zhongnan Hospital of Wuhan University, Wuhan, Hubei 430071, PR China
[10]Hubei Provincial Clinical Research Center for Minimally Invasive Diagnosis and Treatment of Hepatobiliary and Pancreatic Diseases, Wuhan, Hubei 430071, PR China

Received: 27 October 2024 / Accepted: 30 April 2025
Published online: 16 May 2025

References

1. Siegel RL, Giaquinto AN, Jemal A. Cancer statistics, 2024. CA Cancer J Clin. 2024;74(1):12–49.
2. Liu X, Xia F, Chen Y, Sun H, Yang Z, Chen B, et al. Chinese expert consensus on refined diagnosis, treatment, and management of advanced primary liver cancer (2023 edition). Liver Res. 2024;8(2):61–71.
3. He Y, Luo L, Shan R, Qian J, Cui L, Wu Z, et al. Development and validation of a nomogram for predicting postoperative early relapse and survival in hepatocellular carcinoma. J Natl Compr Canc Netw. 2023;22(1D):e237069.
4. Wei H, Luo S, Bi Y, Liao C, Lian Y, Zhang J, et al. Plasma microRNA-15a/16-1-based machine learning for early detection of hepatitis B virus-related hepatocellular carcinoma. Liver Res. 2024;8(2):105–17.
5. Cheng Y, Gong Y, Chen X, Zhang Q, Zhang X, He Y, et al. Injectable adhesive hemostatic gel with tumor acidity neutralizer and neutrophil extracellular traps lyase for enhancing adoptive NK cell therapy prevents post-resection recurrence of hepatocellular carcinoma. Biomaterials. 2022;284:121506.
6. Wang J, Yu H, Dong W, Zhang C, Hu M, Ma W et al. N6-Methyladenosine-Mediated Up-Regulation of FZD10 Regulates Liver Cancer Stem Cells' Properties and Lenvatinib Resistance Through WNT/β-Catenin and Hippo Signaling Pathways. Gastroenterology. 2023;164(6).
7. Park DJ, Sung PS, Kim J-H, Lee GW, Jang JW, Jung ES et al. EpCAM-high liver cancer stem cells resist natural killer cell-mediated cytotoxicity by upregulating CEACAM1. J Immunother Cancer. 2020;8(1).
8. Cunningham TD, Jiang X, Shapiro DJ. Expression of high levels of human proteinase inhibitor 9 blocks both Perforin/granzyme and Fas/Fas ligand-mediated cytotoxicity. Cell Immunol. 2007;245(1):32–41.
9. Chu J, Gao F, Yan M, Zhao S, Yan Z, Shi B, et al. Natural killer cells: a promising immunotherapy for cancer. J Transl Med. 2022;20(1):240.
10. Joshi S, Sharabi A. Targeting myeloid-derived suppressor cells to enhance natural killer cell-based immunotherapy. Pharmacol Ther. 2022;235:108114.
11. Tang F, Tie Y, Tu C, Wei X. Surgical trauma-induced immunosuppression in cancer: recent advances and the potential therapies. Clin Transl Med. 2020;10(1):199–223.
12. Yu SJ, Ma C, Heinrich B, Brown ZJ, Sandhu M, Zhang Q, et al. Targeting the crosstalk between cytokine-induced killer cells and myeloid-derived suppressor cells in hepatocellular carcinoma. J Hepatol. 2019;70(3):449–57.
13. Bugide S, Gupta R, Green MR, Wajapeyee N. EZH2 inhibits NK cell-mediated antitumor immunity by suppressing CXCL10 expression in an HDAC10-dependent manner. Proc Natl Acad Sci U S A. 2021;118:30.
14. Lv J, Wei Y, Yin J-H, Chen Y-P, Zhou G-Q, Wei C, et al. The tumor immune microenvironment of nasopharyngeal carcinoma after gemcitabine plus cisplatin treatment. Nat Med. 2023;29(6):1424–36.
15. Hong C, Wang D, Liang J, Guo Y, Zhu Y, Xia J, et al. Novel ginsenoside-based multifunctional liposomal delivery system for combination therapy of gastric cancer. Theranostics. 2019;9(15):4437–49.
16. Sun S, Tang Q, Wang Y, Zhang L, Chen J, Xu M et al. In situ Micro-Nano conversion augmented Tumor-Localized immunochemotherapy. ACS Appl Mater Interfaces. 2022.
17. Gong Y, Chen W, Chen X, He Y, Jiang H, Zhang X, et al. An injectable epigenetic autophagic modulatory hydrogel for boosting umbilical cord blood NK cell therapy prevents postsurgical relapse of Triple-Negative breast Cancer. Adv Sci (Weinh). 2022;9(23):e2201271.
18. Zhu J-Q, Wu H, Li X, Li M-Y, Li Z-L, Xu X-F, et al. Hydrogel crosslinked with nanoparticles for prevention of surgical hemorrhage and recurrence of hepatocellular carcinoma. Adv Sci (Weinh). 2024;11(9):e2305508.
19. Zhou L, Fan L, Zhang F-M, Jiang Y, Cai M, Dai C, et al. Hybrid gelatin/oxidized chondroitin sulfate hydrogels incorporating bioactive glass nanoparticles

with enhanced mechanical properties, mineralization, and osteogenic differentiation. Bioact Mater. 2021;6(3):890–904.
20. Xin Peng XX, Deng Y, Xie X, Xu L, Xu X, Yuan W, Yang B, Yang X. Xianfeng Xia, Li Duan, and liming Bian. Ultrafast Self-Gelling and wet adhesive powder for acute hemostasis and wound healing. Adv Funct Mater. 2021;31(33).
21. Zhou C, Weng J, Liu C, Liu S, Hu Z, Xie X, et al. Disruption of SLFN11 Deficiency-Induced CCL2 signaling and macrophage M2 polarization potentiates Anti-PD-1 therapy efficacy in hepatocellular carcinoma. Gastroenterology. 2023;164(7):1261–78.
22. Ohira M, Ohdan H, Mitsuta H, Ishiyama K, Tanaka Y, Igarashi Y, et al. Adoptive transfer of TRAIL-expressing natural killer cells prevents recurrence of hepatocellular carcinoma after partial hepatectomy. Transplantation. 2006;82(12):1712–9.
23. Kim JM, Cho SY, Rhu J, Jung M, Her JH, Lim O, et al. Adjuvant therapy using ex vivo-expanded allogenic natural killer cells in hepatectomy patients with hepatitis B virus related solitary hepatocellular carcinoma: MG4101 study. Ann Hepatobiliary Pancreat Surg. 2021;25(2):206–14.
24. Liu Y, Hao Y, Chen J, Chen M, Tian J, Lv X, et al. An injectable puerarin depot can potentiate chimeric antigen receptor natural killer cell immunotherapy against targeted solid tumors by reversing tumor immunosuppression. Small. 2024;20(25):e2307521.
25. Kim W-J, Shin H-L, Kim B-S, Kim H-J, Ryoo H-M. RUNX2-modifying enzymes: therapeutic targets for bone diseases. Exp Mol Med. 2020;52(8):1178–84.
26. Knutson TP, Truong TH, Ma S, Brady NJ, Sullivan ME, Raj G, et al. Posttranslationally modified progesterone receptors direct ligand-specific expression of breast cancer stem cell-associated gene programs. J Hematol Oncol. 2017;10(1):89.
27. Yan X, Han D, Chen Z, Han C, Dong W, Han L, et al. RUNX2 interacts with BRG1 to target CD44 for promoting invasion and migration of colorectal cancer cells. Cancer Cell Int. 2020;20:505.
28. Drissi H, Pouliot A, Koolloos C, Stein JL, Lian JB, Stein GS, et al. 1,25-(OH)2-vitamin D3 suppresses the bone-related Runx2/Cbfa1 gene promoter. Exp Cell Res. 2002;274(2):323–33.
29. Zhang Y, Bush X, Yan B, Chen JA. Gemcitabine nanoparticles promote antitumor immunity against melanoma. Biomaterials. 2019;189:48–59.
30. Sasso MS, Lollo G, Pitorre M, Solito S, Pinton L, Valpione S, et al. Low dose gemcitabine-loaded lipid nanocapsules target monocytic myeloid-derived suppressor cells and potentiate cancer immunotherapy. Biomaterials. 2016;96:47–62.
31. Pinton L, Magri S, Masetto E, Vettore M, Schibuola I, Ingangi V, et al. Targeting of immunosuppressive myeloid cells from glioblastoma patients by modulation of size and surface charge of lipid nanocapsules. J Nanobiotechnol. 2020;18(1):31.
32. Zhao XF, Wang Q, Sun J, Zhang AM, Chang XY, Li WG, et al. [A mechanistic study of radiotherapy on intratumoral NK cell infiltration augmentation by regulating the EZH2/CXCL10 pathway in hepatocellular carcinoma cells]. Zhonghua Gan Zang Bing Za Zhi. 2024;32(9):835–44.
33. Knelson EH, Ivanova EV, Tarannum M, Campisi M, Lizotte PH, Booker MA, et al. Activation of Tumor-Cell STING primes NK-Cell therapy. Cancer Immunol Res. 2022;10(8):947–61.
34. Zhang Z, Zhang C. Regulation of cGAS-STING signalling and its diversity of cellular outcomes. Nat Rev Immunol. 2025.
35. Li Y, Zhu J, Zhang X, Li Y, Zhang S, Yang L, et al. Drug-Delivery nanoplatform with synergistic regulation of Angiogenesis-Osteogenesis coupling for promoting vascularized bone regeneration. ACS Appl Mater Interfaces. 2023;15(14):17543–61.
36. Wang Q, Sun Y, Li S, Zhang P, Yao Q. Synthesis and modification of ZIF-8 and its application in drug delivery and tumor therapy. RSC Adv. 2020;10(62):37600–20.
37. Sang D, Lin K, Yang Y, Ran G, Li B, Chen C et al. Prolonged sleep deprivation induces a cytokine-storm-like syndrome in mammals. Cell. 2023;186(25).
38. Zhang Z, Kuang G, Zong S, Liu S, Xiao H, Chen X, et al. Sandwich-Like fibers/sponge composite combining chemotherapy and hemostasis for efficient postoperative prevention of tumor recurrence and metastasis. Adv Mater. 2018;30(49):e1803217.
39. Huang S, Wang Z, Zhou J, Huang J, Zhou L, Luo J, et al. EZH2 inhibitor GSK126 suppresses antitumor immunity by driving production of Myeloid-Derived suppressor cells. Cancer Res. 2019;79(8):2009–20.
40. Lee J, Kang TH, Yoo W, Choi H, Jo S, Kong K, et al. An antibody designed to improve adoptive NK-Cell therapy inhibits pancreatic Cancer progression in a murine model. Cancer Immunol Res. 2019;7(2):219–29.
41. Lu W, Cao F, Feng L, Song G, Chang Y, Chu Y, et al. LncRNA Snhg6 regulates the differentiation of MDSCs by regulating the ubiquitination of EZH2. J Hematol Oncol. 2021;14(1):196.
42. Liu J, Lin W-P, Su W, Wu Z-Z, Yang Q-C, Wang S, et al. Sunitinib attenuates reactive MDSCs enhancing anti-tumor immunity in HNSCC. Int Immunopharmacol. 2023;119:110243.
43. Hasan SS, Rizvi A, Naseem I. Calcitriol-induced DNA damage: toward a molecular mechanism of selective cell death. IUBMB Life. 2013;65(9):787–92.
44. Prabagar MG, McQueney M, Bommireddy V, Siegel R, Schieven GL, Lu K et al. THE STING AGONIST VB-85247 INDUCES DURABLE ANTITUMOR IMMUNE RESPONSES BY INTRAVESICAL ADMINISTRATION IN A NON-MUSCLE INVASIVE BLADDER CANCER. Cancer Res. 2024.
45. Dagher OK, Posey AD. Forks in the road for CAR T and CAR NK cell cancer therapies. Nat Immunol. 2023;24(12):1994–2007.
46. Hao J, Chen C, Pavelic K, Ozer F. ZIF-8 as a pH-Responsive nanoplatform for 5-Fluorouracil delivery in the chemotherapy of oral squamous cell carcinoma. Int J Mol Sci. 2024;25(17).
47. Qu J, Zhao X, Ma PX, Guo B. pH-responsive self-healing injectable hydrogel based on N-carboxyethyl Chitosan for hepatocellular carcinoma therapy. Acta Biomater. 2017;58:168–80.
48. Gao B, Luo J, Liu Y, Su S, Fu S, Yang X, et al. Intratumoral administration of thermosensitive hydrogel Co-Loaded with Norcantharidin nanoparticles and doxorubicin for the treatment of hepatocellular carcinoma. Int J Nanomed. 2021;16:4073–85.
49. Zhu AX, Blaszkowsky LS, Ryan DP, Clark JW, Muzikansky A, Horgan K, et al. Phase II study of gemcitabine and oxaliplatin in combination with bevacizumab in patients with advanced hepatocellular carcinoma. J Clin Oncol. 2006;24(12):1898–903.

Publisher's note